

# 1 MAX-DOAS observations of formaldehyde and nitrogen dioxide at three 2 sites in Asia and comparison with the global chemistry transport model 3 CHASER

4 Hossain Mohamed Syedul Hoque<sup>1</sup>, Kengo Sudo<sup>1,2</sup>, Hitoshi Irie<sup>3</sup>, Alessandro Damiani<sup>3</sup>, Manish Naja<sup>4</sup>, and Al  
5 Mashroor Fatmi<sup>3</sup>

6 <sup>1</sup>Graduate School of Environmental Studies, Nagoya University, Nagoya, 4640064, Japan

7 <sup>2</sup>Japan Agency for Marine-Earth Science and Technology (JAMSTEC), Kanagawa, 2370061, Japan

8 <sup>3</sup>Center for Environmental Remote Sensing (CEReS), Chiba University, Chiba, 2638522, Japan

9 <sup>4</sup>Aryabhatta Research Institute for Observational Sciences (ARIES), Manora Peak, Nainital-263001, Uttarakhand,  
10 India

11

12 *Correspondence to:* Hossain Mohammed Syedul Hoque (hoque.hossain.mohammed.syedul.u6@f.mail.nagoya-  
13 u.ac.jp or hoquesyedul@gmail.com)

14

15 **Abstract.** Formaldehyde (HCHO) and nitrogen dioxide (NO<sub>2</sub>) concentrations and profiles were retrieved  
16 from ground-based multi-axis differential optical absorption spectroscopy (MAX-DOAS) observations  
17 during January 2017 - December 2018 at three sites in Asia: (1) Phimai (15.18°N, 102.5°E), Thailand;  
18 (2) Pantnagar (29°N, 78.90°E) in the Indo Gangetic Plain (IGP), India; and (3) Chiba (35.62°N,  
19 140.10°E), Japan. Retrievals were performed using the Japanese MAX-DOAS profile retrieval algorithm  
20 ver. 2 (JM2). The observations were used to evaluate the NO<sub>2</sub> and HCHO partial columns and profiles (0  
21 - 4 km) simulated using the global chemistry transport model (CTM) CHASER. The NO<sub>2</sub> and HCHO  
22 concentrations at all three sites showed consistent seasonal variation throughout the investigated period.  
23 Biomass burning affected the HCHO and NO<sub>2</sub> variations at Phimai during the dry season and at Pantnagar  
24 during spring (March - May) and post-monsoon (September - November). Results found for the HCHO  
25 to NO<sub>2</sub> ratio ( $R_{FN}$ ), an indicator of high ozone sensitivity, indicate that the transition region (i.e.,  $1 < R_{FN}$   
26  $< 2$ ) changes regionally, echoing the recent finding for  $R_{FN}$  effectiveness. Moreover, reasonable estimates  
27 of transition regions can be derived, accounting for the NO<sub>2</sub> - HCHO chemical feedback.

28 The model was evaluated against global NO<sub>2</sub> and HCHO columns data retrieved from Ozone Monitoring  
29 Instrument (OMI) observations before comparison with ground-based datasets. Despite underestimation,  
30 the model well simulated the satellite-observed global spatial distribution of NO<sub>2</sub> and HCHO, with  
31 respective spatial correlations ( $r$ ) of 0.73 and 0.74. CHASER demonstrated good performance,  
32 reproducing the MAX-DOAS retrieved HCHO and NO<sub>2</sub> abundances at Phimai, mainly above 500 m from  
33 the surface. Model results agree with the measured variations within the one sigma standard deviation of  
34 the observations. Simulations at higher resolution improved the modeled NO<sub>2</sub> estimates for Chiba,  
35 reducing the mean bias error (MBE) for the 0 - 2 km height by 35%, but resolution-based improvements  
36 were limited to surface layers. Sensitivity studies show that at Phimai, pyrogenic emissions contribute to  
37 HCHO and NO<sub>2</sub> concentrations up to 50 and 35%, respectively.

## 38 **1 Introduction**

39 Formaldehyde (HCHO), the most abundant carbonyl compound in the atmosphere, is a high-yield product  
40 of oxidization of all primary volatile organic compounds (VOCs) emitted from natural and anthropogenic  
41 sources by hydroxyl radicals (OH). Oxidation of long-lived VOCs such as methane produces a global  
42 HCHO background concentration of 0.2 – 1.0 ppbv in remote marine environments (Weller et al., 2000;  
43 Burkert et al., 2001; Singh et al., 2004; Sinreich et al., 2005). Aside from oxidation of VOCs, the  
44 significant sources of HCHO are direct emissions from biomass burning, industrial processes, fossil fuel  
45 combustion (Lee et al., 1997; Hak et al., 2005; Fu et al., 2008), and vegetation (Seco et al., 2007).  
46 However, oxidization of non-methane VOCs emitted from biogenic (e.g., isoprene) or anthropogenic (e.g.,  
47 butene) sources govern the spatial variation of HCHO on a global scale (Franco et al., 2015). The sinks  
48 of HCHO include photolysis at wavelengths shorter than 400 nm, oxidation by OH, and wet deposition,  
49 thereby limiting the lifetime of HCHO to a few hours (Arlander et al., 1995).

50 Nitrogen dioxide (NO<sub>2</sub>), an important atmospheric constituent, (1) participates in the catalytic  
51 formation of tropospheric ozone (O<sub>3</sub>), (2) acts as a catalyst for stratospheric ozone (O<sub>3</sub>) destruction  
52 (Crutzen, 1970), (3) contributes to the formation of aerosols (Jang and Kamens, 2001), (4) acts as a  
53 precursor of acid rain (Seinfeld and Pandis, 1998), and (5) strongly affects radiative forcing (Solomon et  
54 al. 1999; Lelieveld et al., 2002;). Nitrogen oxides (NO<sub>x</sub> = NO (nitric oxide) + NO<sub>2</sub>) are emitted from  
55 natural and anthropogenic sources. Primary NO<sub>x</sub> emission sources include biomass burning, fossil fuel

56 combustion, soil emissions, and lightning (Bond et al., 2001; Zhang et al., 2003). Not only do  $\text{NO}_x$   
57 emissions degrade air quality; they are leading air pollutant (Ma et al., 2013). Both HCHO and  $\text{NO}_2$  are  
58 important intermediates in the global VOC– $\text{HO}_x$  (hydrogen oxides)– $\text{NO}_x$  catalytic cycle, which governs  
59  $\text{O}_3$  chemistry in the troposphere (Lee et al., 1997; Houweling et al., 1998; Hak et al., 2005; Kanakidou et  
60 al., 2005). Thus, both trace gases play crucially important roles in tropospheric chemistry.

61 The observational sites examined for the present study have different atmospheric characteristics.  
62 Thailand is strongly affected by pollution because of rapid economic development and urbanization.  
63 Moreover, biomass burning in Southeast Asia is a significant source of  $\text{O}_3$  precursors, contributing up to  
64 30% of the total concentrations during the peak burning season (Amnuaylorajen et al., 2020; Khodmanee  
65 et al. 2021). Because of rapid industrialization, India the second most populous country in the world, is  
66 witnessing an increasing  $\text{O}_3$  trend along with  $\text{NO}_2$  and HCHO concentrations in all major cities (Mahajan  
67 et al; 2015; Lu et al, 2018;). The Indo-Gangetic Plain (IGP), which covers ~21% of the Indian  
68 subcontinent land area is hotspots of severe air pollution (Giles et al; 2005, Biswas et al; 2019). In contrast,  
69 surface  $\text{O}_3$  concentrations have shown an increasing trend in Japan, despite decreasing  $\text{NO}_x$  and VOC  
70 concentrations related to emission control measures after 2000 (Irie et al., 2021). Therefore, observational  
71 and modeling studies must be conducted to improve our quantitative understanding of the  $\text{O}_3$ - $\text{NO}_x$ -VOC  
72 relation in these regions.

73 Multi-axis differential optical absorption spectroscopy (MAX-DOAS), a well-established, unique, and  
74 powerful remote sensing method for measuring trace gases and aerosols, is based on the DOAS technique.  
75 Aerosols and trace gases are quantified using selective narrowband (high frequency) absorption features  
76 (Platt 1994; Platt and Stutz 2008). Spectral radiance measurements at different elevation angles (ELs) can  
77 provide profile information about atmospheric trace gases and aerosols (Hönninger et al., 2004; Wagner  
78 et al., 2004; Wittrock et al., 2004; Frieß et al., 2006; Irie et al., 2008a). Many studies have demonstrated  
79 the retrieval of aerosol and trace gas concentrations and profiles from MAX-DOAS observations,  
80 including  $\text{NO}_2$  and HCHO (Clémer et al., 2010; Irie et al., 2011; Hendrick et al., 2014; Wang et al., 2014;  
81 Franco et al., 2015; Frieß et al., 2016).

82 The ability of MAX-DOAS to provide information related to surface concentrations, vertical profiles,  
83 and column densities makes it a good complement to ground-based in situ and satellite observations.

Moreover, the MAX-DOAS method uses narrowband absorption of the target compounds, thereby obviating any need for radiometric calibration of the instrument. Because of these advantages, MAX-DOAS systems are deployed for the assessment of aerosol and trace gases in regional and global observational networks such as BREDOM (Wittrock et al., 2004), BIRA-IASB (Cl  mer et al., 2010), and MADRAS (Kanaya et al., 2014). Such datasets are used, in but are not limited to, (1) air quality assessment and monitoring, (2) evaluation of chemistry-transport models (CTMS), and (3) validation of satellite data retrievals. Several studies have used MAX-DOAS datasets to validate tropospheric columns retrieved from satellite observations, including NO<sub>2</sub> and HCHO (Irie et al., 2008b; Ma et al., 2013; Chan et al., 2020; Ryan et al., 2020). However, limited MAX-DOAS datasets have been used to evaluate global CTMs. Vigouroux et al. (2009) and Franco et al. (2015) respectively used the MAX-DOAS HCHO datasets from Reunion Island and Jungfraujoch stations to evaluate the Intermediate Model of Annual and Global Evolution of Species (IMAGES) and GEOS-Chem model simulations. Kanaya et al. (2014) validated the Model for Interdisciplinary Research on Climate–Earth System Model – Chemistry (MIROC-ESM-CHEM) simulated NO<sub>2</sub> column densities with MAX-DOAS observations in Cape Hedo and Fukue in Japan. Kumar et al. (2021) used MAX-DOAS observations to evaluate the high-resolution regional model Meco(n)(MESSy-field ECHAM and COSMO model nested n times).

For this study, NO<sub>2</sub> and HCHO profiles retrieved from MAX-DOAS observations from the International air quality and sky research remote sensing (A-SKY) (<http://atmos3.cr.chiba-u.jp/a-sky/>) network sites are used to evaluate the global Chemical Atmospheric General Circulation Model for the Study of Atmospheric Environment and Radiative Forcing (CHASER; Sudo et al., 2002). The three A-SKY sites of - (1) Phimai in Thailand (15.18  N, 102.56  E), (2) Pantnagar (29  N, 78.90  E) in the IGP in India, and (3) Chiba (35.62  N, 140.10  E) in Japan, are respectively representative of rural, semi-rural, and urban environments. CHASER has been used mostly for global-scale research (Sudo et al., 2007; Sekiya et al., 2014, 2018; Miyazaki et al., 2017). The study described herein is the first reported attempt to evaluate the CHASER-simulated NO<sub>2</sub> and HCHO profiles using MAX-DOAS observations in three different atmospheric environments. Moreover, few reports of the literature have described the use of MAX-DOAS datasets to evaluate global CTMs in South Asia and South-east Asia. Overall, this study was conducted

111 to provide important insights into model performances and to help reduce model uncertainties related to  
112 NO<sub>2</sub> and HCHO simulations in these regions.

113 The paper is structured in the following manner. First, the observation sites, MAX-DOAS  
114 instrumentation, and retrieval strategies are described in section 2. Section 2 also includes a short  
115 description of the CHASER model and Ozone Monitoring Instrument (OMI) HCHO and NO<sub>2</sub> retrievals.  
116 Next, the observations and the evaluation results are described in sections 3. Finally, the sensitivity study  
117 results are provided in section 3.4. and the concluding remarks in section 4.

118

119

## 120 **2 Observations, datasets, and methods**

121

### 122 **2.1 Site Information**

123 Continuous MAX-DOAS observations at Chiba, Phimai, and Pantnagar started respectively in 2012,  
124 2014, and 2017. The measurements from January 2017 to December 2018 at all three sites are discussed  
125 herein. Phimai, a rural site, is located ~260 km north-east of the Bangkok metropolitan area and is unlikely  
126 to be affected by vehicular and industrial emissions. However, the site is affected by biomass burning  
127 during January - April. Two major air streams: the dry, cool north-east monsoon during November – mid-  
128 February and the wet, warm south-west monsoon during mid-May – September affect the climate in  
129 Phimai. As described by, Hoque et al. (2018), the climate classifications of Phimai are the (a) dry season  
130 (January – April), and (b) wet season (June – September).

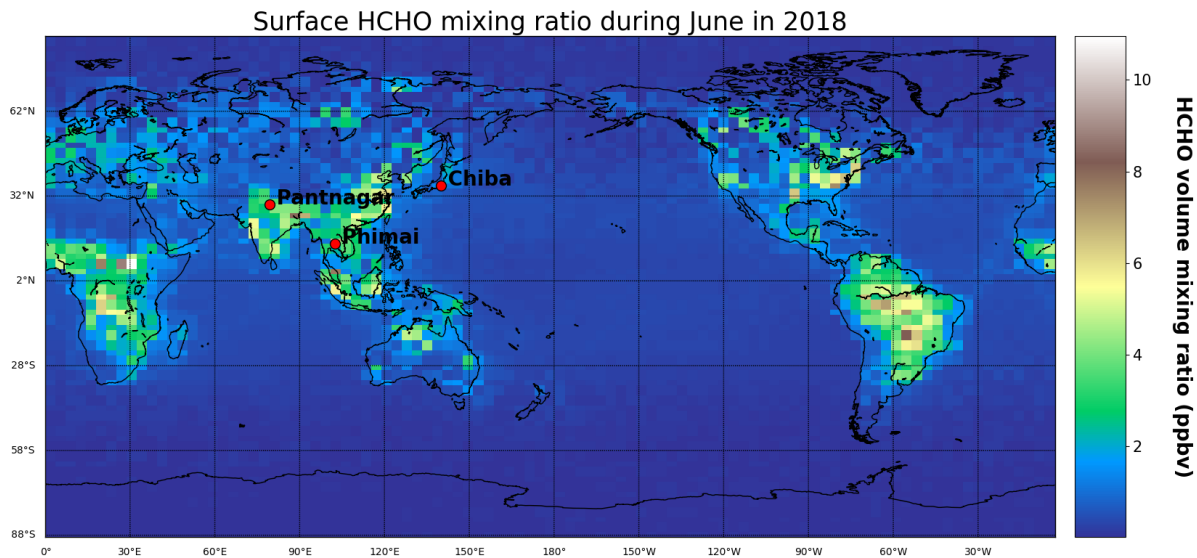
131 Pantnagar, a semi-urban site in India, is located in the IGP. The Indian capital of New Delhi is situated  
132 at ~225 km south-west of the site. The low-altitude plains are on the south and west sides of the site. The  
133 Himalayan mountains are located to the north and east. An important roadway with moderate traffic  
134 volume and a small local airport lies within 3 km of the site. Rudrapur (~12 km south-west of Pantnagar)  
135 and Haldwani (~ 25 km north-east of Pantnagar) are the two major cities near Pantnagar, where non-  
136 combustible industries are located (Joshi et al., 2016). The climate classification at Pantnagar is the

137 following: (1) winter (December–February), (2) spring (March–May), (3) summer monsoon (June–  
138 August), and (4) autumn (September–November).

139 Chiba, an urban site, is located ~40 km south-east of the Tokyo metropolitan region. Tokyo Bay,  
140 large-scale industries, and residential areas are located within a 50 km radius. Chiba has four distinct  
141 seasons: (1) spring (March–May), (2) summer (June–August), (3) autumn (September–November), and  
142 winter (December– February). The locations of the three sites are depicted in Fig. 1.

143

144



145 **Figure 1:** Surface HCHO mixing ratio in June 2018, simulated using the CHASER model. The red points  
146 represent the locations of the observation sites, which are part of the A-SKY network.

147

148

## 149 2.2 MAX-DOAS retrieval

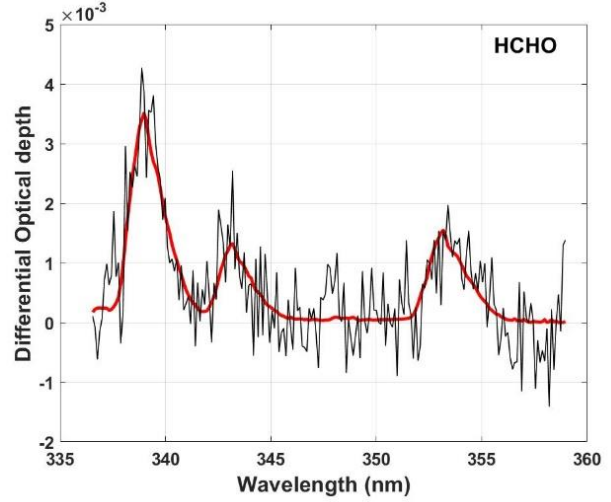
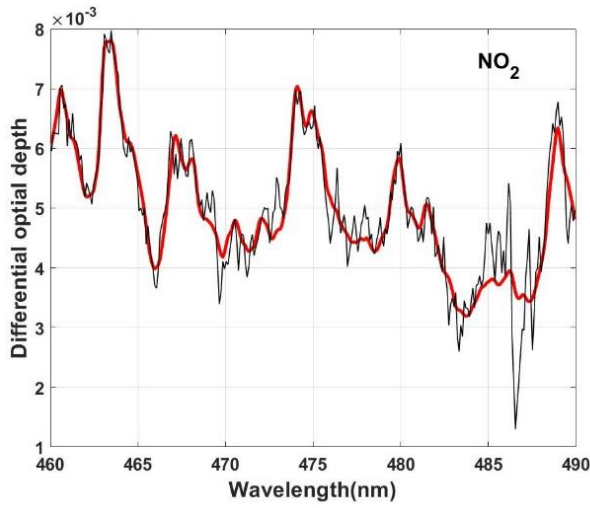
150 The MAX-DOAS systems used for continuous observations at the three sites participated in the Cabauw  
151 Intercomparison Campaign of Nitrogen Dioxide measuring Instruments (CINDI) (Roscoe et al., 2010)  
152 and CINDI-2 (Kreher et al., 2020) campaigns. The instrumentation setup is described by Irie et al. (2008,  
153 2011, 2015). The indoor part of the MAX-DOAS systems consists of an ultraviolet-visible (UV-VIS)  
154 spectrometer (Maya2000Pro; Ocean Optics Inc.) embedded in a temperature-controlled box. The outdoor  
155 unit consists of a single telescope and a 45° inclined movable mirror on a rotary actuator, used to perform  
156 reference and off-axis measurements. The high-resolution spectra from 310–515 nm is recorded at six  
157 elevation angles (ELs) of 2°, 3°, 4°, 6°, 8°, and 70° at the Chiba and Phimai sites. At the Pantnagar site,  
158 measurements are conducted at ELs of 3°, 4°, 5°, 6°, 8°, and 70°. The sequences of the ELs at all the sites  
159 were repeated every 15 min. The reference spectra are recorded at EL of 70° instead of 90° to avoid  
160 saturation of intensity. Because all the ELs were considered in the box air mass factor ( $A_{box}$ ) calculation  
161 to retrieve the vertical profile, the choice of reference EL (70° or 90°) is not an important issue for this  
162 study. The off-axis ELs are limited to  $< 10^\circ$  to reduce the systematic error in the in-oxygen collision  
163 complex ( $O_4$ ) fitting results (Irie et al., 2015), thereby maintaining high sensitivity in the lowest layer of  
164 the retrieved aerosol and trace gas profiles. Daily wavelength calibration using the high-resolution solar  
165 spectrum from Kurucz et al. (1984) is performed to account for the spectrometer's long-term degradation.  
166 The spectral resolution (full width half maximum: FWHM) is about 0.4 nm at 357 and 476 nm. The  
167 concentrations and profiles of aerosol and trace gases are retrieved using the Japanese vertical profile  
168 retrieval algorithm (JM2 ver. 2) (Irie et al., 2011, 2015). The algorithm works in three steps: (1) DOAS  
169 fittings, (2) profile/column retrieval of aerosol, and (3) profile/column retrieval of trace gases. Irie et al.  
170 (2008a, 2008b, 2011, 2015) described the retrieval procedures, and the error estimates. Herein we provide  
171 a short overview.

172 First, the differential slant column density ( $\Delta SCD$ ) of trace gases is retrieved using the DOAS  
173 technique (Platt 1994), which uses the nonlinear least-squares spectral fitting method, according to the  
174 following equation :

$$\ln I(\lambda) = \ln(I_o(\lambda) - c(\lambda)) - \sum_i^n \sigma_i(\lambda) \Delta SCD_i - p(\lambda) \quad (1)$$

Therein,  $I_o(\lambda)$  represents the reference spectrum measured at time  $t$ .  $I_o(\lambda)$  is derived by interpolating two reference spectra (i.e., EL=70°) within 15 min before and after the complete sequential scan of the off-axis ELs at time  $t$ .  $\Delta SCD$  represents the difference between the slant column density along the off-axis and reference spectrum. Second- and third-order polynomials are fitted to account, respectively, the wavelength-dependent offset  $c(\lambda)$  and the effect of molecular and particle scattering  $p(\lambda)$ . In addition,  $c(\lambda)$  accounts for the influence of stray light. The HCHO  $\Delta SCD$  and NO<sub>2</sub>  $\Delta SCD$  are retrieved respectively, from the fitting windows of 340–370 and 460–490 nm. Significant O<sub>4</sub> absorptions in the 338–370 and 460–490 nm fitting windows are used to retrieve the O<sub>4</sub>  $\Delta SCD$ s. The absorption cross-section data sources and the fitted absorbers in the HCHO and NO<sub>2</sub> fitting windows are given in Table 1. Figure 2 presents an example of the fitting results. O<sub>4</sub> fittings in both retrieval windows are shown in Fig S1 (supplementary information).





188 **Figure 2:** Examples of spectral fitting of NO<sub>2</sub> and HCHO, where red and black lines respectively show the scaled  
 189 cross-section and the summation of scaled cross-sections and fitting residuals. The example shows the  
 190 measurements of 10 April 2017, in Phimai at 10:00 LT at an EL of 2°.

191 In the second step, the aerosol optical depth (AOD)  $\tau$  and the vertical profiles of the aerosol extinction  
 192 coefficient (AEC)  $k$  are retrieved using the approach developed by Irie et al, (2008a) which is based on  
 193 the optimal estimation method (Rogers, 2000). In this approach, the measurement vector  $y$  (representing  
 194 the quantities to be fitted) and state vector (representing the retrieved quantities) is defined as

195

$$196 \quad y = (O_4 \Delta SCD(\Omega_1) \dots \dots \Delta SCD(\Omega_n))^T \quad (2) \text{ and}$$

$$197 \quad x = (\tau F_1 F_2 F_3)^T \quad (3),$$

198

200 **Table 1.** Cross-section data references and absorbers fitted in the HCHO and NO<sub>2</sub> windows

Cross-section	Absorbers fitted	Data Source
O <sub>3</sub>		Bougmil et al. (2003), 223K
NO <sub>2</sub>	O <sub>3</sub> , NO <sub>2</sub> , H <sub>2</sub> O, O <sub>4</sub> , Ring	Vandaele et al. (1996), 295K
BrO		Fleischmann et al. (2004), 223K
Ring		Chance and Spurr (1997)
H <sub>2</sub> O		Vandaele et al. (2005), 280K
O <sub>4</sub>		Hermans et al. (2003), 296K
HCHO	O <sub>3</sub> , NO <sub>2</sub> , HCHO, BrO, O <sub>4</sub> , Ring	Meller and Moortgart (2000), 293k

201

202

203 where  $n$  stands for the number of measurements within one complete scan of an EL sequence. Also,  $\Omega$   
204 denotes the viewing geometry and includes three components: solar zenith angle (SZA), EL, and relative  
205 azimuth angle (RAA). The  $F$  values determine the profile shape, with values between 0 and 1. The partial  
206 AOD for 0–1, 1–2, 2–3, and above 3 km layers were defined respectively as  $AOD \cdot F_1$ ,  $AOD \cdot (1-F_1) F_2$ ,  
207 and  $AOD \cdot (1-F_1) (1-F_2) F_3$ , and  $AOD \cdot (1-F_1) (1-F_2) (1-F_3)$ . The AEC profile from 3 to 100 km is derived

208 assuming a fixed value at 100 km and exponential AEC profile shape with a scaling height of ~1.6 km.  
 209 The  $k$  value at 100 km was estimated from Stratospheric Aerosol and Gas Experiment III (SAGE III)  
 210 aerosol data ( $\lambda=448$  and 521 nm) taken at altitudes of 15–40 km. The negligible influence of such  
 211 assumptions on the retrievals in the lower troposphere has been demonstrated in sensitivity studies  
 212 reported by Irie et al (2012). Similarly, the AEC profiles at 2–3, 1–2, and 0–1 km were derived. Such  
 213 parameterization provides the advantage that the AEC profile can be retrieved using only the apriori  
 214 knowledge of the  $F$  values (profile shape) and little or no information related to the absolute AEC values  
 215 in the troposphere. Irie et al. (2008a) demonstrated that the relative variability of the profile shape, in  
 216 terms of 1-km averages, is smaller than that of the absolute AEC values. AEC profile shapes  
 217 corresponding to different  $F$  values is shown in Fig.S2 (supplementary information). However, the  
 218 vertical resolution and the measurement sensitivity cannot be derived directly with such a  
 219 parameterization (Irie et al., 2008a; 2009). The retrievals and simulations conducted by other groups for  
 220 similar geometries (i.e., Frieß et al., 2006) are used to overcome such limitations. The apriori values used  
 221 for this study were similar to those reported by Irie et al. (2011):  $AOD = 0.21 \pm 3.0$ ,  $F_1 = 0.60 \pm 0.05$ ,  $F_2$   
 222  $= 0.80 \pm 0.03$ , and  $F_3 = 0.80 \pm 0.03$ .

223 Then, a lookup table (LUT) of the box air mass factor ( $A_{box}$ ) vertical profile at 357 and 476 nm is  
 224 constructed using the radiative transfer model JACOSPAR (Irie et al., 2015), which is based on the Monte  
 225 Carlo Atmospheric Radiative Transfer Simulator (MCARaTS) (Iwabuchi, 2006). The values of the single-  
 226 scattering albedo ( $s$ ), asymmetry parameter ( $g$ ), and surface albedo were, respectively, 0.95, 0.65 (under  
 227 the Henyey-Greenstein approximation), and 0.10. The U.S. standard atmosphere temperature and pressure  
 228 profiles were used for radiative transfer calculations. Uncertainty of less than 8% related to the usage of  
 229 fixed values of  $s$ ,  $g$ , and  $a$  were estimated from sensitivity studies (i.e., Irie et al 2012). Results obtained  
 230 from JACOSPAR are validated in the study reported by Wagner et al. (2007). The optimal aerosol load  
 231 and the  $A_{box}$  profiles are derived using the  $A_{box}$  LUT and the  $O_4$   $\Delta$ SCD at all ELs.

232 In the third step, the  $A_{box}$  profiles, HCHO and  $NO_2$   $\Delta$ SCDs, and the nonlinear iterative inversion  
 233 method are used to retrieve the HCHO and  $NO_2$  vertical column densities (VCDs) and profiles. Here the  
 234  $NO_2$  retrieval is explained.

235

For trace gas retrieval, the measurement vector and state vector are defined as

$$y = (NO_2\Delta SCD(\Omega_1) \dots \dots NO_2\Delta SCD(\Omega_n))^T \quad (4) \text{ and}$$

$$x = (VCD f_1 f_2 f_3)^T \quad (5)$$

VCD represents the vertical column density below 5 km. The  $f$  values are the profile shape factors. Above the 5 km layer, fixed profiles are assumed. Similarly, to aerosol retrieval, the partial VCD values for the 0–1, 1–2, 2–3, and 3–5 km is defined respectively as  $VCD \cdot f_1$ ,  $VCD \cdot (1-f_1) f_2$ ,  $VCD \cdot (1-f_1) (1-f_2) f_3$ , and  $VCD \cdot (1-f_1) (1-f_2) (1-f_3)$ . Finally, the volume mixing ratio (VMR) is calculated using the partial VCD, and U.S. standard atmosphere temperature and pressure data scaled to the respective surface measurements.

The calculated vertical profile is converted to  $NO_2$   $\Delta SCDs$  using the  $A_{box}$  LUT constructed for aerosol retrieval. However, the trace gas wavelengths differed from the representative wavelengths of  $A_{box}$  LUT (357 and 476 nm). Therefore, the AOD at the trace gas wavelength is estimated, converting the retrieved AOD to the closer aerosol wavelength of 357 or 476 nm, assuming the Angstrom exponent value of 1.00. The choice of the Angstrom exponent value can induce uncertainty in the retrieved VCDs. However, such uncertainty was found to be non-significant compared to that of  $A_{box}$  profiles. Uncertainty in the  $A_{box}$  profiles are assumed to be as high as 30 to 50%. Such values are derived empirically from comparison with sky radiometer and LIDAR observations (i.e., Irie et al., 2008b). Then, the  $A_{box}$  profiles from the LUT corresponding to the recalculated AOD values are selected. The dependence of the  $A_{box}$  profiles on the concentration profiles is expected to be low because both HCHO and  $NO_2$  are optically thin absorbers (Wagner et al., 2007; Irie et al., 2011). For every 15 min (time necessary for one complete scan of ELs), 20% (the mean ratio of the retrieved VCD to maximum  $\Delta SCD$ ) of the maximum trace gas  $\Delta SCDs$  is used as a priori information for the VCD retrievals. The a priori error is set to 100% of the maximum trace gas  $\Delta SCD$ . Figure 3 presents the mean averaging kernel (AK) of the HCHO and  $NO_2$  retrievals during the dry season at Phimai. The area (Rodgers, 2000) provides an estimate of the measurement contribution to the retrieval. The total area is the sum of all the elements in the AK and weighted by the a priori error (Irie et al. 2008a). The areas for VCD and  $f_1$  of  $NO_2$  retrieval are 1 and 0.6, respectively. The  $f_2$  and  $f_3$  values are much smaller. Consequently, at first, the a priori profiles were scaled, and later  $f$  values determined

the profile shape. The VCD area is close to unity, and therefore, the retrieved VCD is independent of the a priori values. Irie et al (2008) conducted sensitivity studies of choice of the  $f$  values and reported negligible effect on the retrievals.

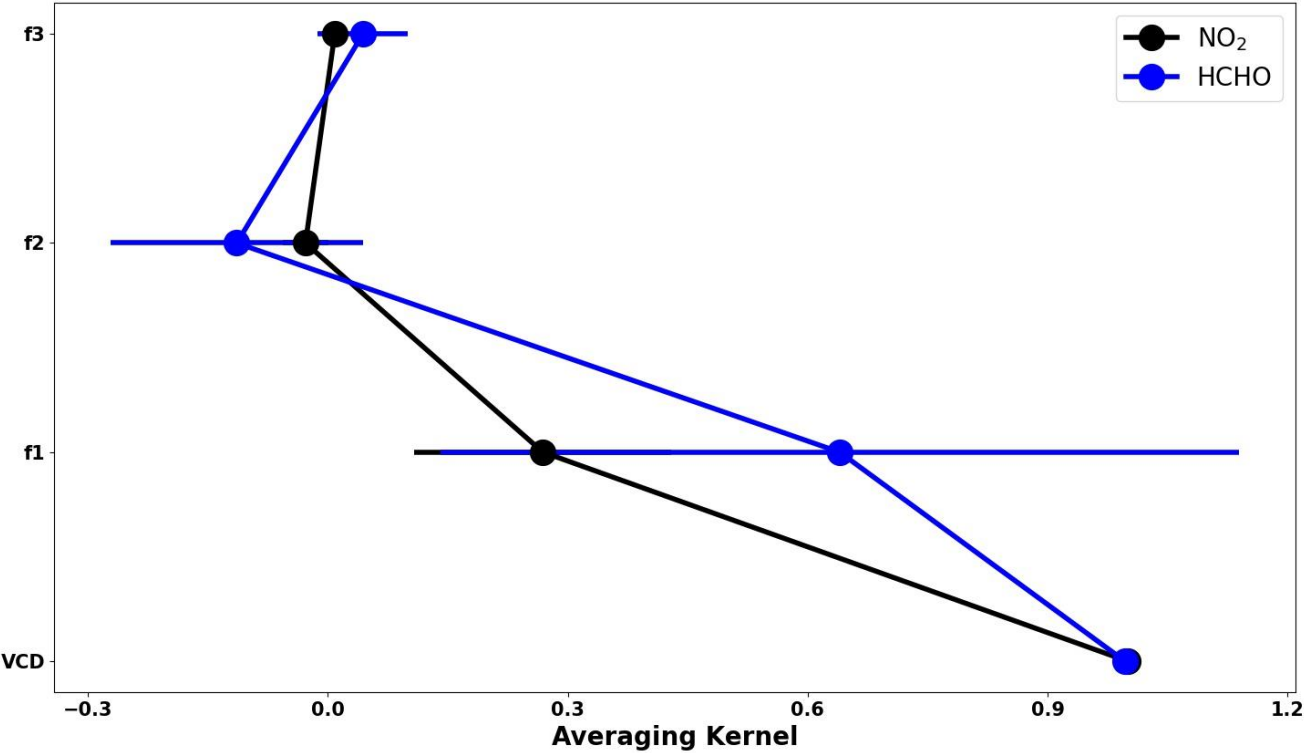


**Figure 3:** Mean averaging kernel of the NO<sub>2</sub> and HCHO retrievals from observations at Phimai during 2017. The error bars represent the 1-sigma standard deviation of the mean values.

The total error of the retrieval consists of random and systematic errors. The measurement error covariance matrix constructed from the residuals of the respective trace gas  $\Delta$ SCDs is used to estimate the random error. The systematic error is calculated while assuming uncertainties as high as 30 and 50% in the retrieved AOD (or the corresponding  $A_{box}$  values). Table 2 shows the total estimated error. Aside from the random and systematic error, more sources of error might exist. For instance, the bias in the ELs

277 can induce uncertainties in the retrieved products. However, Hoque et al. (2018) demonstrated that such  
278 biases had a non-significant effect on the final retrieved products, mostly less than 5%.

279 The cloud screening procedure is similar to that described by Irie et al. (2011) and by Hoque et al.  
280 (2018a, 2018b). During the retrieval steps, retrieved AOD values greater than 3 are excluded, because  
281 optically thick clouds are primarily responsible for such large optical depth. Filtering based on the  
282 residuals of O<sub>4</sub> and the trace gas ΔSCDs is also used to screen clouds. Larger residuals likely occur due  
283 to two reasons: (1) when the constructed profile is too simple to represent the true profile, particularly  
284 with a steep vertical gradient of extinction due to clouds, and (2) rapid changes in optical depth within 30  
285 min (time for one complete scan) (Irie et al, 2011).The screening criteria are: respective residuals of O<sub>4</sub>,  
286 HCHO, and NO<sub>2</sub> ΔSCDs < 10%, < 50%, and <20%, and the degrees of freedom of retrievals greater than  
287 1.02. The threshold values were determined statistically corresponding to the mode plus one sigma (1σ)  
288 in the logarithmic histogram of relative residuals.

289  
290 **Table 2.** Estimated Errors (%) for the NO<sub>2</sub> and HCHO concentration in 0-1 km layer, retrieved using the  
291 JM2 algorithm

Retrieved Product	Random error	Systematic error	Error related to instrumentation	Total error
NO <sub>2</sub>	10	12	5	16
HCHO	16	25	5	30

292  
293  
294 **2.3 CHASER simulations**

295 CHASER 4.0 (Version 4) (Sudo et al., 2002; Sudo and Akimoto, 2007; Sekiya and Sudo, 2014), coupled  
296 online with the MIROC-AGCM atmospheric general circulation model (AGCM) (K-1 model developers,  
297 2004) and the SPRINTARS aerosol transport model (Takemura et al., 2005, 2009), is a global chemistry  
298 transport model used to study the atmospheric environment and radiative forcing. In addition, several

299 updates, including the introduction of aerosol species (sulfate, nitrate, etc.) and related chemistry,  
 300 radiation, and cloud processes, have been implemented in the latest version of CHASER.  
 301 CHASER can calculate the concentrations of 92 species through 263 chemical reactions (gaseous,  
 302 aqueous, and heterogeneous chemical reactions) considering the chemical cycle of  $O_3$ – $HO_x$  –  $NO_x$  – $CH_4$ –  
 303  $CO$  along with oxidation of non-methane volatile organic compounds (NMVOCs)(Miyazaki et al., 2017).  
 304 The chemical mechanism is largely based on the master chemical mechanism (MCM,  
 305 <http://mcm.york.ac.uk>)(Jenkin et al., 2015). CHASER simulates the stratospheric  $O_3$  chemistry  
 306 considering the Chapman mechanisms, catalytic reactions related to halogen oxides ( $HO_x$ ,  $NO_x$ ,  $ClO_x$ ,  
 307 and  $BrO_x$ ), and polar stratospheric clouds (PSCs). Resistance-based parameterization (Wesely, 1989),  
 308 cumulus convection, and large-scale condensation parameterizations are used to calculate dry and wet  
 309 depositions. The piecewise parabolic method (Colella and Woodward, 1984)

310

311 **Table 3:** Settings of the CHASER simulations used in this study

Simulation	Anthropogenic emissions	Pyrogenic emissions	Biogenic emissions	Soil NO <sub>x</sub> emission	Other physical and chemical processes
Standard	ON	ON	ON	ON	ON
L1_HCHO	ON	Pyrogenic VOCs switched	ON	ON	ON
L1_opt	ON	OFF	Reduced by 50%	ON	ON
L1_NO <sub>2</sub>	ON	ON	ON	OFF	ON

---

<b>L2</b>	Anthropogenic	ON	ON	ON	ON
	VOC emissions				
	switched OFF				

---

312

313 and the flux-form semi-Lagrangian schemes (Lin and Rood, 1996) calculate advective tracer transport.  
 314 CHASER simulates tracer transport on a sub-grid scale in the framework of the prognostic Arakawa–  
 315 Schubert cumulus convection scheme (Emori et al., 2001) and the vertical diffusion scheme (Mellor and  
 316 Yamada, 1974). In this study, CHASER simulations were conducted at a horizontal resolution of  $2.8^\circ \times$   
 317  $2.8^\circ$ , with 36 vertical layers from the surface to ~50 km altitude and a typical time step of 20 min. The  
 318 meteorological fields simulated by MIROC-AGCM were nudged toward the six-hourly NCEP FNL  
 319 reanalysis data at every model time step.

320 The anthropogenic, biomass burning, lightning, and soil emissions of  $\text{NO}_x$  were incorporated into  
 321 CHASER simulations. Anthropogenic emissions were based on HTAP\_v2.2 for 2008. Biomass burning  
 322 and soil emissions from the ECMWF/MAC (Global Fire Assimilation System (GFAS)) reanalysis were  
 323 used. The biogenic emissions for VOCs are based on the process-based biogeochemical model the  
 324 Vegetation Integrative Simulator for Trace gases (VISIT) (Ito and Inatomi, 2012) simulations. The  $\text{NO}_x$   
 325 production from lightning is calculated based on the parameterization of Price and Rind (1992) linked to  
 326 the convection scheme of the AGCM (Sudo et al., 2002). Isoprene, terpene, acetone, and ONMV  
 327 emissions estimates in the VISIT inventory during July were  $2.14 \times 10^{-11}$ ,  $4.43 \times 10^{-12}$ ,  $1.60 \times 10^{-12}$ , and  
 328  $9.93 \times 10^{-13} \text{ kgCm}^{-2}\text{s}^{-1}$ . Global  $\text{NO}_x$  emissions of  $43.80 \text{ TgNyr}^{-1}$  are used in the simulations, considering  
 329 industries ( $23.10 \text{ TgNyr}^{-1}$ ), biomass burning ( $9.65 \text{ TgNyr}^{-1}$ ), soil ( $5.50 \text{ TgNyr}^{-1}$ ), lightning ( $5 \text{ TgNyr}^{-1}$ ),  
 330 and aircrafts ( $0.55 \text{ TgNyr}^{-1}$ ) as significant sources. Global isoprene emissions from vegetation were set to  
 331  $400 \text{ TgCyr}^{-1}$ .



NO<sub>x</sub> emissions in India were estimated as 14 Tg/yr in 2016, almost two-fold increase since 2005 (~8 Tg/yr), with the energy and transportation sector being the largest contributor (Sadavarte et al 2014). Indian anthropogenic non-methane VOCs (NMVOCs) emissions in 2010 were estimated ~ 10 Tg/yr, with respective contributions of 60, 16, and 12% from residential, solvents, and the transport sector (Sharma et al 2015). In Japan, vehicular exhausts (14 - 25%), gasoline vapor (9 - 16%), liquefied natural gas (7 - 10%), and liquefied petroleum gas (49 - 71%) contribute to the total VOC concentrations (Morino et al., 2011), with annual NMVOC emission of ~2 Tg (Kannari et al., 2007). Annual NO<sub>x</sub> emissions in Japan and Thailand in 2000 was estimated as ~2000 and 591 kt/yr, with the largest contribution from transport-oil use, followed by the energy and industrial sector (Ohara et al., 2007). Annual anthropogenic VOC emissions in Thailand are approximately 0.9 Tg, with 43, 38, and 20% contributed, respectively, from industrial, residential and transportation sectors (Woo et al; 2020). Multiple CHASER simulations with different settings used for sensitivity studies are presented in Table 3.

345

## 2.4 Satellite observations

Tropospheric NO<sub>2</sub> and HCHO retrievals from the Ozone monitoring Instrument (OMI) were also used to evaluate the model simulations. The ultra-violet nadir-viewing spectrometer OMI, on board the Aura satellite measures backscattering solar radiation covering the spectral range of 270 – 500 nm (Levelt et al., 2006). In an ascending sun-synchronous polar-orbit, OMI crosses the equator at 13:40 LT (local time) (Zara et al., 2018). OMI measures at a spatial resolution of 13 × 24 km<sup>2</sup> and provides daily global coverage of various trace gases including NO<sub>2</sub> and HCHO. The NO<sub>2</sub> and HCHO datasets were obtained respectively from the TEMIS ([www.temis.nl](http://www.temis.nl), last accessed on 2022/04/23) and aeronomie (<https://h2co.aeronomie.be/>, last accessed 2022/05/03) websites. NO<sub>2</sub> tropospheric columns retrieved using the DOMINO version 2.0 (Boersma et al., 2011) algorithm were used for the analysis. Data meeting the following criteria were selected: cloud fraction < 0.5, SZA < 70°, surface albedo < 0.3, quality flags = 0, and cross-track quality flags = 0. For HCHO, we used the BIRA-IASB v14 (De Smedt et al 2015)

358 retrieved products. The data filtering criteria was the following: cloud fraction < 0.4, SZA<70°, AMF >  
359 0.2, quality flag=0, and cross-track quality flag =0.

360

361

## 362 **3 Results and discussion**

### 363 **3.1 Results from MAX-DOAS observations**

#### 364 **3.1.1 HCHO seasonal variation**

365 The monthly mean HCHO mixing ratios in the 0–1 and 0–2 km layers from January 2017 – December  
366 2018 and the corresponding one sigma ( $1\sigma$ ) standard deviations indicating the variation ranges for the  
367 three sites are presented in Fig. 4. The HCHO levels at the Phimai site show a consistent seasonal cycle,  
368 characterized by high VMRs during the dry season. Such enhancement is related to the influence of  
369 biomass burning during the dry season, which has been well documented in the work of Hoque et al.  
370 (2018). The HCHO mixing ratio at Phimai reach a peak in March or April, with a maximum of 4 – 6  
371 ppbv. The variation in the peak concentration and timing depends mainly on the intensity of biomass  
372 burning activities. During the wet season, the HCHO concentrations are mostly within 2–3 ppbv,  
373 indicating a two-fold increase in HCHO abundances during the dry season. The daily mean HCHO  
374 amounts (0 –1 km) are 0.78 - 9.84 ppbv, representing seasonal modulation of 134%.

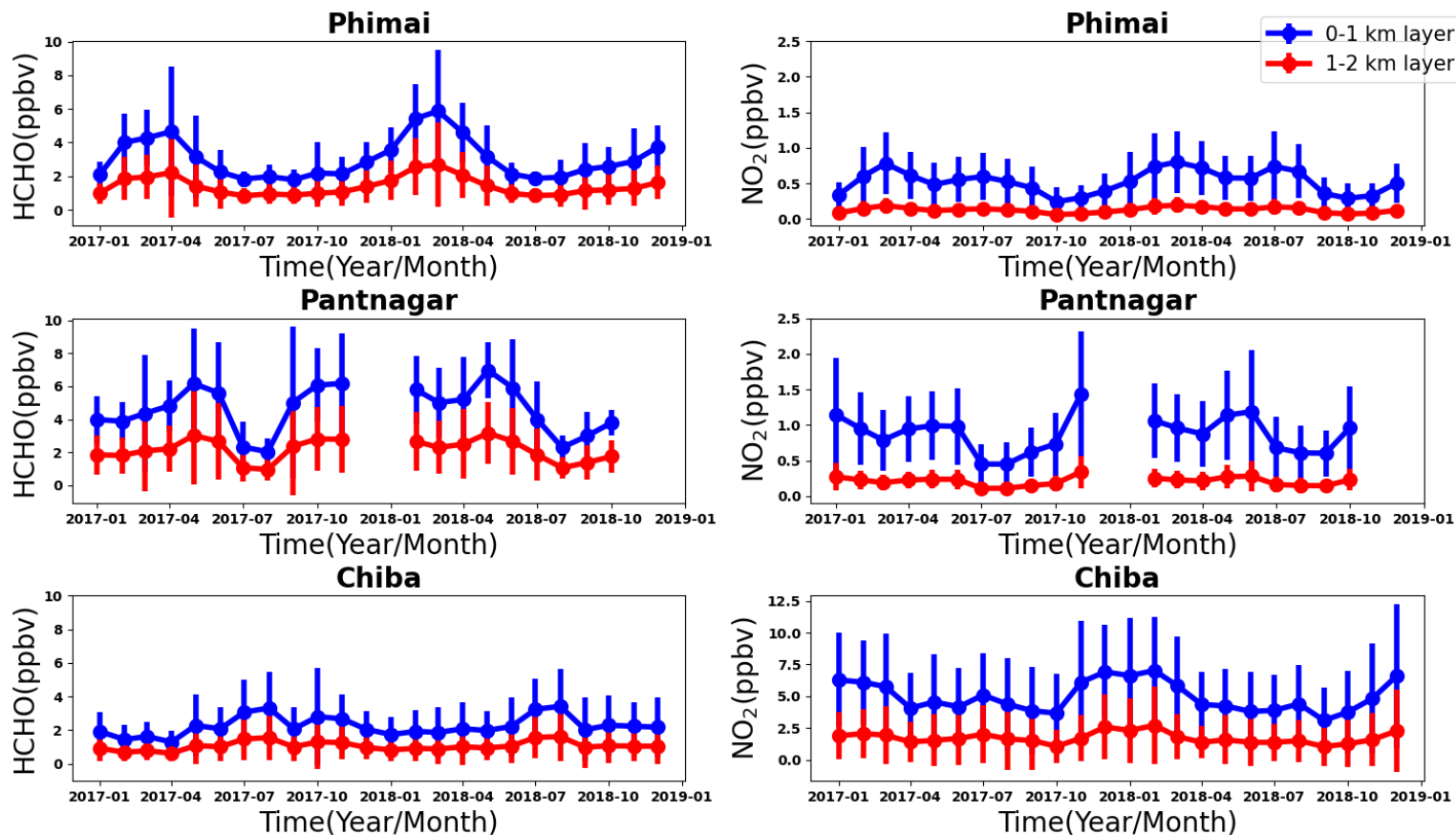


**Figure 4:** Seasonal variations in the HCHO (left panel) and NO<sub>2</sub> (right panel) mixing ratios in the 0 - 1 (blue) and 1 - 2 (red) km layers at Phimai, Pantnagar, and Chiba. The error bars represent the one sigma standard deviation of the mean values. The gaps in the plots for the Pantnagar site indicate the unavailability of observations during the investigated period.

380

381

Seasonal variation of HCHO in the 0–1 km layer at the Pantnagar site has been elucidated by Hoque et al. (2018b). Here, the results are replotted to verify the consistency of the seasonal variations. Observations made during autumn 2018 were not available because of problem with the spectrometer. Consistent seasonal variation of HCHO abundances is observed at the Pantnagar site, with enhanced concentrations during the spring. The Pantnagar site is affected by biomass burning during spring and autumn (Hoque et al., 2018b), explaining the high mixing ratios found during spring. In both years, the

388 maximum HCHO mixing ratios are  $\sim 6$  ppbv. The springtime peak occurred in May. The HCHO  
389 concentrations during the monsoon are  $\sim 35\%$  lower than in the spring, indicating a strong effect of the  
390 monsoon on the HCHO concentrations found for Pantnagar. The seasonal modulation of HCHO at  
391 Pantnagar estimated from the daily mean concentrations is 107%. The peak HCHO mixing ratio at  
392 Pantnagar is almost twice that of in Pune city ( $\sim 3$  ppbv) (Biswas and Mahajan, 2021), a site in the IGP  
393 region. The HCHO seasonality at the two sites are found to be dissimilar, because of differences in the  
394 VOC sources, however, lower mixing ratios during the monsoon is consistent. From another site in the  
395 IGP region (i.e., Mohali), Kumar et al., (2020) reported lowest HCHO VCDs during March 2014 and  
396 2015, attributing them to lower biogenic and anthropogenic VOC emissions. At Pantnagar, the lowest  
397 HCHO mixing ratios are observed during the monsoon. The rainfall events in the IGP region shows strong  
398 annual variability (Fukushima et al. 2019). Discrepancies between the sites might be related to the rainfall  
399 pattern.

400 Under the influence of biomass burning, the maximum monthly HCHO mixing ratios at Phimai and  
401 Pantnagar are similar ( $\sim 6$  ppb). The maximum instantaneous HCHO VMR during biomass burning  
402 influence in Phimai and Pantnagar are, respectively, 26 and 30 ppbv. Zarzana et al. (2017) reported HCHO  
403 abundances of  $\sim 60$  ppbv in fresh biomass plumes in the US. The lower values obtained from our  
404 measurements might be attributable to (1) more aged plumes intercepted by the MAX-DOAS instruments  
405 and (2) differences in the types of biomass fuel used. Comparison to reports of literature indicates that the  
406 retrieval of HCHO under biomass burning is reasonable.

407 The summertime maximum and wintertime minimum characterize the seasonal variations of HCHO at  
408 the Chiba site, with a peak at  $\sim 3$  ppbv. The HCHO concentrations are  $\sim 2$  ppbv during other seasons,  
409 which are similar to the HCHO concentrations in Phimai during the wet season. The seasonal variation  
410 amplitudes of HCHO at Chiba is  $\sim 94\%$ . For a site with similar seasonal variation (i.e., summertime  
411 maximum and wintertime minimum), Franco et al. (2015) reported HCHO seasonal modulation of 88%.

412 The HCHO VMRs in the 1–2 km layers at all three sites are lower, almost 50% the value of the  
413 concentrations in the 0–1 km layer. The HCHO seasonal variation amplitudes at Phimai, Pantnagar, and  
414 Chiba sites are, respectively, 131%, 102%, and 90% when calculated based on the HCHO concentration  
415 in the 1–2 km layers. The modulation was even lower when retrieved values for the 2–3 km layer is used.

### 3.1.2 NO<sub>2</sub> seasonal variation at the three sites

Figure 4 also shows the seasonal variation of NO<sub>2</sub> in the 0–1 and 1–2 km layers at the three sites. The error bars represent the 1 $\sigma$  standard deviation of the mean values. The NO<sub>2</sub> seasonal variations at Phimai and Pantnagar sites are similar to those of HCHO. Pronounced peaks attributable to biomass burning influence is observed during the dry season at Phimai (~0.8 ppbv) and during spring (1.2 ppbv), and post-monsoon (1.4 ppbv) at Pantnagar. The lowest NO<sub>2</sub> mixing ratios at Phimai and Pantnagar are, respectively, ~0.2 and 0.5 ppbv. The NO<sub>2</sub> VMRs at Chiba is higher (~7 ppbv) during winter. The longer lifetime of NO<sub>x</sub> and lower NO/NO<sub>2</sub> ratio because of lower photochemical activity in winter lead to high NO<sub>2</sub> mixing ratios at Chiba (Irie et al., 2021).

At Phimai, the NO<sub>2</sub> mixing ratios in both seasons are similar. However, when Hoque et al. (2018a) reported the seasonal variations in NO<sub>2</sub> at Phimai during 2015 – 2018, the dry season mixing ratios were higher. Table 4 shows the number of fire events during the dry seasons during 2015 - 2018. The fire data are extracted from the MODIS Active Fire Detections database (<https://firms.modaps.eosdis.nasa.gov>, last accessed on 2021/12/15). Data fulfilling the following criteria were chosen – (a) data points located within 100 km of the Phimai site, (b) confidence of the data greater than 70%, and (c) observations during the daytime. The lower fire counts during 2017 - 2018 compared to those of 2015 - 2016 period coincide with the lower NO<sub>2</sub> levels in the former. Fire counts varied between 2017 and 2018 but did not affect the NO<sub>2</sub> levels. However, HCHO levels changed with the number of fire occurrences between 2015 – 2018 (i.e., Figure 4 and Hoque et al., 2018a).

At such low NO<sub>2</sub> levels at Phimai, soil NO<sub>x</sub> emissions are likely to make a greater contribution to NO<sub>2</sub>. Although NO<sub>2</sub> is not emitted directly from soils, biological processes emit NO, which is rapidly converted to NO<sub>2</sub> (Hall et al., 1996). In addition, many studies have established a relation between soil moisture and NO emissions (Carden et al., 1993; Zheng et al., 2000; Schindlbacher et al., 2004; Huber et al., 2020). The potential contribution of soil NO<sub>x</sub> emissions, as inferred from CHASER simulations, is discussed in section 3.4.2.

**Table 4:** Number of fire events occurring during the dry season (January - April) at Phimai from 2015 - 2018. Selection criteria of the data are the following: (1) situated within 100 km of the site, (2) confidence level > 70%, and (c) daytime measurements.

Dry season years	Number of fire events
2015	84
2016	98
2017	62
2018	77

### 3.1.3.1 The HCHO to NO<sub>2</sub> ratio ( $R_{FN}$ ):

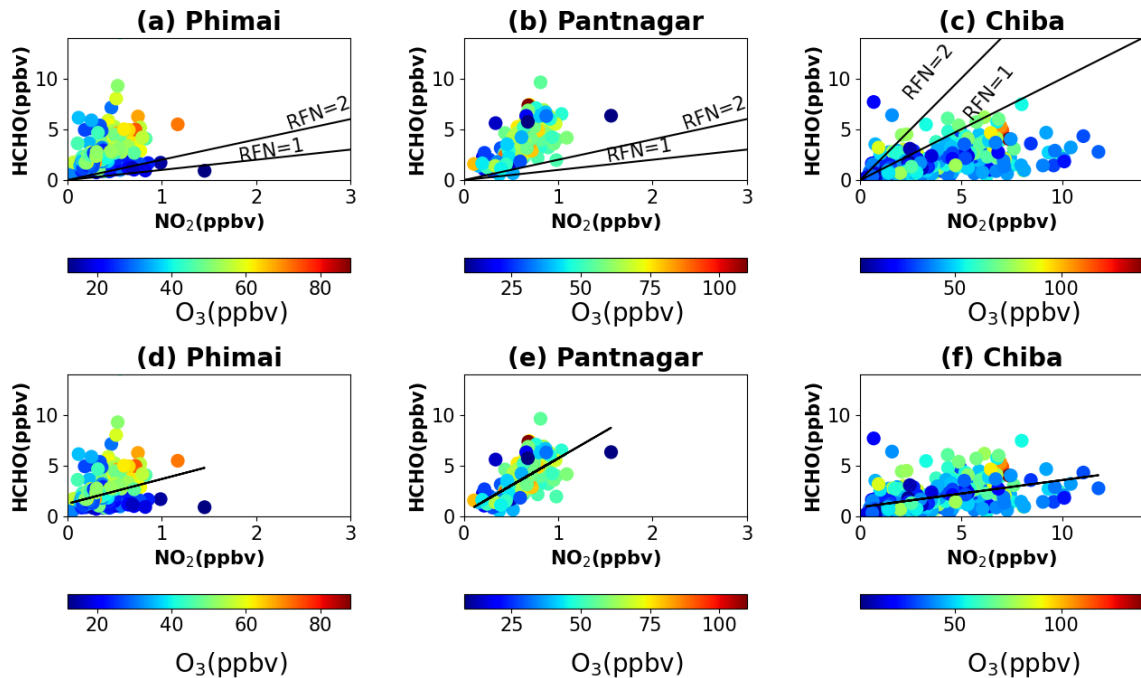
The HCHO to NO<sub>2</sub> ( $R_{FN}$ ) ratio is regarded as an indicator of high ozone O<sub>3</sub> sensitivity (Martin et al., 2004; Duncan et al., 2010). The O<sub>3</sub> production regime is characterized as VOC-limited for  $R_{FN} < 1$  and NO<sub>x</sub>-limited when  $R_{FN} > 2$ , and the values in the range 1-2 are said to be in the transition/ambiguous region (Duncan et al., 2010; Ryan et al., 2020). Subsequent to a report of Tonnesen and Dennis (2000), several studies used  $R_{FN}$  estimated from satellite and ground-based observations to infer O<sub>3</sub> sensitivity to NO<sub>x</sub> and VOCs (Martian et al., 2004; Duncan et al., 2010; Jin and Holloway et al., 2015; Mahajan et al., 2015; Irie et al., 2021; etc.). However, the effectiveness of  $R_{FN}$  is still under discussion primarily based on two-points- (1) the range of the transition region to categorize the VOC and NO<sub>x</sub> -limited region, and (2) the altitude dependence of  $R_{FN}$  (Jin et al., 2017). Most of the studies described above used the transition range ( $1 < R_{FN} < 2$ ) proposed by Duncan et al. (2010). Schroeder et al. (2017) reported that a common transition (i.e.,  $1 < R_{FN} < 2$ ) range might not be valid globally. Instead, it should be calculated based on the region. First, the results based on the standard transition range are discussed herein, and then its applicability to the study regions is assessed.

Figure 5 shows scatter plots of the daily mean NO<sub>2</sub> and HCHO concentrations in the 0 - 2 km layer at the three sites, color-coded with the respective O<sub>3</sub> concentrations (0-2 km). Retrieval of the JM2 O<sub>3</sub> product is explained by Irie et al. (2011). The O<sub>3</sub> concentrations for SZA < 50° are used to minimize stratospheric effects. This criterion on the SZA is also applied for the selection of the NO<sub>2</sub> and HCHO concentrations. Although not checked here, the JM2 O<sub>3</sub> product showed good agreement with ozonesonde measurements in Tsukuba (Irie et al., 2021). Most of the high O<sub>3</sub> occurrences fall in the  $R_{FN} > 2$  region at Phimai and Pantnagar and in  $R_{FN} < 1$  at Chiba. The common transition range classifies the O<sub>3</sub> production regime as

NO<sub>x</sub>-limited at Phimai and Pantnagar and VOC-limited at Chiba. At all sites, the  $R_{FN}$  values tend to be biased to a particular regime (i.e., NO<sub>x</sub> - or VOC-limited), with only 4 and 2% of the ratios in the range 0 - 2, at Phimai and Pantnagar, respectively. This finding suggests that the transition occurs at a higher or lower ratio than the common definition. Recent report by Souri et al. (2020) found that the NO<sub>2</sub>-HCHO relation plays an important role in determining the transition region and derived a formulation from accounting for the NO<sub>2</sub>-HCHO chemical feedback in the ratios as

$$HCHO = m * (NO_2 - b) \quad (6)$$

where m and b respectively denote the slope and intercept. Equation (6) is based on observations, which means that the regionally adjusted fitting coefficients will reflect the local NO<sub>2</sub> - HCHO relation. Solving equation (6), the transition line estimated from the observations in the 0 - 2 km layer, is shown in Fig 5 (bottom panel). Rather than a range, the method calculates a single transition line, which corresponds to the NO<sub>2</sub> - HCHO feedback. The regions above and below the transition line are characterized, respectively as VOC- and NO<sub>x</sub> -limited or other.



481 **Figure 5.** Scatter plots of HCHO and NO<sub>2</sub> concentrations in the 0-2 km layer at (a, d) Phimai, (b, e) Pantnagar, and  
482 (c, f) Chiba, coloured with the O<sub>3</sub> concentrations in the 0-2 km layer at the respective sites. The solid lines in the  
483 top panel represent  $R_{FN} = 2$  and  $R_{FN} = 1$  benchmarks. The black lines in the bottom panel are calculated according  
484 to equation (1).

485

486 The revised transition line at Phimai and Pantnagar is apparently more reasonable than the earlier method.  
487 At Phimai, the transition line almost clearly distinguishes between the high and low O<sub>3</sub> occurrences. It is  
488 perceptible that when the HCHO concentrations are higher than NO<sub>2</sub>, the transition of the regimes is likely  
489 to occur at higher  $R_{FN}$  values. The minimum and mean  $R_{FN}$  value along the transition line are 3.62 and  
490 6.78, respectively. Because Phimai is a VOC-rich environment, the regime transition occurs at higher  $R_{FN}$   
491 values than by the conventional definition. This finding echoes the results reported by Schroeder et al.  
492 (2017) for a regionally variable transition region. The definition of  $R_{FN} < 1$  as a VOC -limited regime might  
493 not be valid in this case. Considering the mean  $R_{FN}$  ratio along the transition line (i.e., 6.78), the VOC-  
494 and NO<sub>x</sub> -limited (and other) regimes are defined, respectively as  $R_{FN} < 6.78$  and  $R_{FN} > 6.78$ . Based on this  
495 definition, around 34% (65%) of the ratios are higher (lower) than 6.78, classifying Phimai as a dominant  
496 VOC-limited region, which contradicts earlier results. Biomass burning affects Phimai during January -  
497 April and is a significant emission source in addition to biogenic emissions. Thus, high O<sub>3</sub> occurrences  
498 likely occur only 30% of the time during a year. Such events mostly lie above the transition line.

499 At Pantnagar, high O<sub>3</sub> occurrences lie below (42%) and above (57%) the transition line, indicating that  
500 O<sub>3</sub> production is sensitive to both HCHO and NO<sub>2</sub> which contradicts results reported by Biswas et al.  
501 (2019). Based on satellite and ground-based observations, the study estimated the  $R_{FN}$  values at a site in  
502 the IGP as  $> 4$  and  $> 2$  respectively, and regarded the O<sub>3</sub> regime as NO<sub>x</sub>-limited. Mahajan et al. (2015)  
503 reported  $R_{FN}$  values of less than 1 over the IGP region signifying as a VOC-limited region. Pantnagar is  
504 a sub-urban site situated beside a busy road. Therefore, effects of anthropogenic emissions are expected  
505 year-round, especially with pyrogenic emissions during the spring and post-monsoon period. O<sub>3</sub>  
506 sensitivity to both NO<sub>x</sub> and VOCs in the north-west IGP region has also been reported by Kumar and  
507 Sinha (2021). Therefore, the balance between the VOC and NO<sub>x</sub>-limited region in the IGP is reasonable.  
508 The mean and minimum  $R_{FN}$  value along the transition line are, respectively, 5.59 and 6.09. The minimum



509 value (i.e., 5.59) is higher than Phimai (3.26), suggesting higher VOC levels at Pantnagar, consistent with  
510 the observations.

511 At Chiba, 60% of the  $R_{FN}$  values lie below the transition line, suggesting a dominant VOC-limited  
512 region, which is consistent with the results reported by Irie et al. (2021). The minimum and the mean  $R_{FN}$   
513 along the transition line are, respectively, 0.33 and 0.72. The transition occurs at a low  $R_{FN}$  value because  
514 of higher  $\text{NO}_2$  levels. The fact that, 40% of the  $R_{FN}$  values are above the transition region suggests a  
515 moderate effect of HCHO on the  $\text{O}_3$  sensitivity at Chiba.

516 Although the new classification results are apparently reasonable, they should be interpreted with  
517 care. Our current understanding of  $R_{FN}$  contradicts the classification of rural sites as VOC-limited. Despite  
518 the theoretical and observational evidence (i.e., Souri et al., 2020), the classification of regimes based on  
519 a single transition line is not yet well-established. Schroder et al. (2017) used regionally varying transition  
520 ranges. Moreover, (a) the number of observations and (b) the systematic and retrieval errors can affect  
521 the estimations and classifications. These findings are expected to contribute to the ongoing discussion  
522 about the effectiveness of  $R_{FN}$ . However, the results support the idea of a regionally varying transition  
523 range.

524

### 525 3.1.3.2 $R_{FN}$ profiles

526 Figure 6 shows the seasonal mean  $R_{FN}$  profiles at the three sites. Only the profiles during the high  $\text{O}_3$   
527 concentrations at the sites (i.e., March at Phimai, May at Pantnagar, and February at Chiba) are shown.  
528 The  $R_{FN}$  values are likely increase with height because of the lower vertical gradient of  $\text{NO}_2$ , than that of  
529 HCHO (Fig.4). It is particularly interesting that, the  $R_{FN}$  values are similar in the 1-2 km height under  
530 biomass burning conditions, suggesting a small variation in the HCHO loss rate in the particular layer. At  
531 both sites, the HCHO concentration at 1.5 km is about 3 ppbv. At Chiba, a considerable amount of  $\text{NO}_2$   
532 in the higher layers increases the ratio up to 2 km height. Beyond 2 km, the ratio variation at all sites is  
533 opposite that found for the surface. The gradient issue of  $R_{FN}$  has been discussed explicitly by Jin et al.  
534 (2017). They proposed a conversion factor to account for gradient differences in the surface and column-  
535 derived  $R_{FN}$  values, estimating the conversion factor from the model simulated surface and column

536 abundances of NO<sub>2</sub> and HCHO. We adopt the method reported by Jin et al. (2017) for this study using  
537 the CHASER simulated NO<sub>2</sub> and HCHO concentrations and vertical columns.

538 First, CHASER simulated near-surface NO<sub>2</sub> and HCHO concentrations were converted to number  
539 density. The effective boundary layer height (E) (Halla et al., 2011; Jin et al., 2017) was estimated.

540

541 
$$E_{NO_2} = \frac{NO_2 \text{ total column}}{NO_2 \text{ near-surface number density}} \quad (7)$$

542

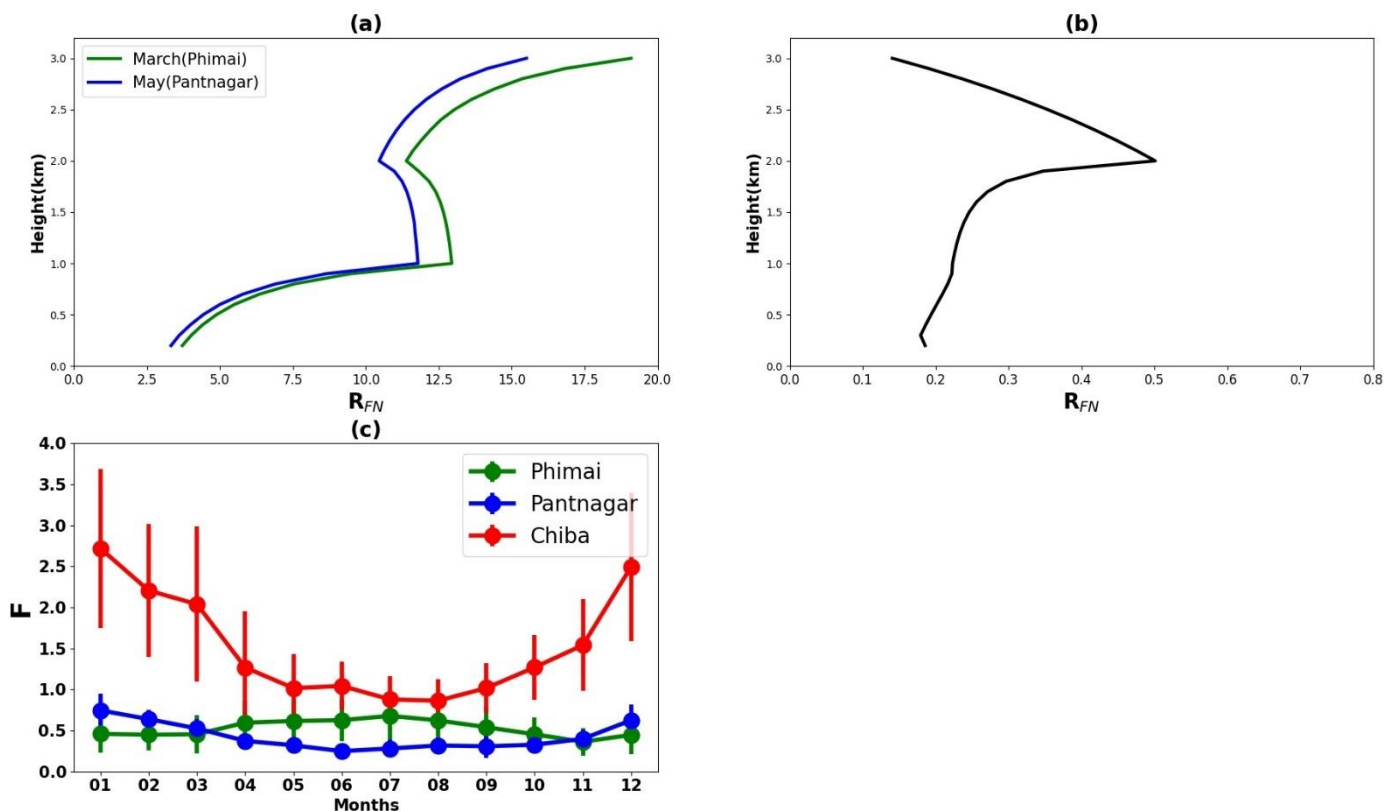
543 
$$E_{HCHO} = \frac{HCHO \text{ total column}}{HCHO \text{ near-surface number density}} \quad (8)$$

544 Therein, E<sub>NO<sub>2</sub></sub> and E<sub>HCHO</sub> respectively denote the effective boundary layer heights of NO<sub>2</sub> and HCHO.

545 In the second step, the column to surface conversion factor (F) was calculated according to the following  
546 equation:

547 
$$F = \frac{E_{HCHO}}{E_{NO_2}} \quad (9)$$

548 The seasonal variation of F for the three A-SKY sites and the associated 1σ standard deviation of the  
549 mean values are depicted in Fig. 7(c). The F values over East Asia reported by Jin et al. (2017) were ~2,  
550 without marked seasonal variation. CHASER estimated F values over Chiba range between 1–2.5, which  
551 is apparently reasonable, when compared with literature values. Values reported in literature for polluted  
552 regions (NO<sub>2</sub> > 2.5 molecules cm<sup>-2</sup>) considered simulation data for 1–2 PM, but the estimates for this  
553 study used daytime (07:00 – 18:00) simulations.



554

555 **Figure 6:** Seasonal mean  $R_{FN}$  profiles during (a) March and May at Phimai and Pantnagar, respectively, and (b)  
 556 February at Chiba. (c) Seasonal variations in the column to surface conversion factor (F) for the Phimai, Pantnagar,  
 557 and Chiba sites, estimated from the CHASER simulated HCHO and NO<sub>2</sub> surface concentrations and VCD. The  
 558 simulated data from 07:00 – 18:00 in 2017 were used to estimate the F values. The error bars represent the one  
 559 sigma standard deviation of the mean values.

560

561 The F values for Pantnagar are mostly less than 1, with no distinctive seasonal variation. Mahajan et  
 562 al. (2015) reported OMI-derived  $R_{FN}$  values < 1 over the IGP region. When this estimated conversion  
 563 factor is used with the values reported by Mahajan et al. (2015), the discrepancy in the satellite and  
 564 ground-based observation derived  $R_{FN}$  values in the IGP region are reduced indicating that the estimated  
 565 F values for the Pantnagar site can be representative for the IGP region. The F values at the Phimai site

range were 0.5–1. Our estimated F values for the Phimai and Pantnagar sites are useful as representative values for these respective regions, which can be improved further based on the results.

### 3.2 Global Evaluation of the CHASER model

This section describes the evaluation of CHASER NO<sub>2</sub> and HCHO columns for 2017 against OMI observations. The OMI AKs were applied to the CHASER outputs to account for the altitude-dependence of the retrievals. First, 2-hourly simulated profiles (NO<sub>2</sub> and HCHO) were sampled closest to the observation time. Secondly, AKs were applied to the sampled profiles and the mean profile was calculated. Thirdly, both the simulations and observations were averaged on a 2.8° bin grid. The month of July and December were discarded from the NO<sub>2</sub> comparison because few coincident days (only five days) were available after filtering. It should be noted that simulations based on old NO<sub>x</sub> emission inventory will likely affect the model-satellite comparison results. However, the current study has not assessed such impact due to technical issues related to using an updated emission inventory. All these issues will be addressed in a separate study.

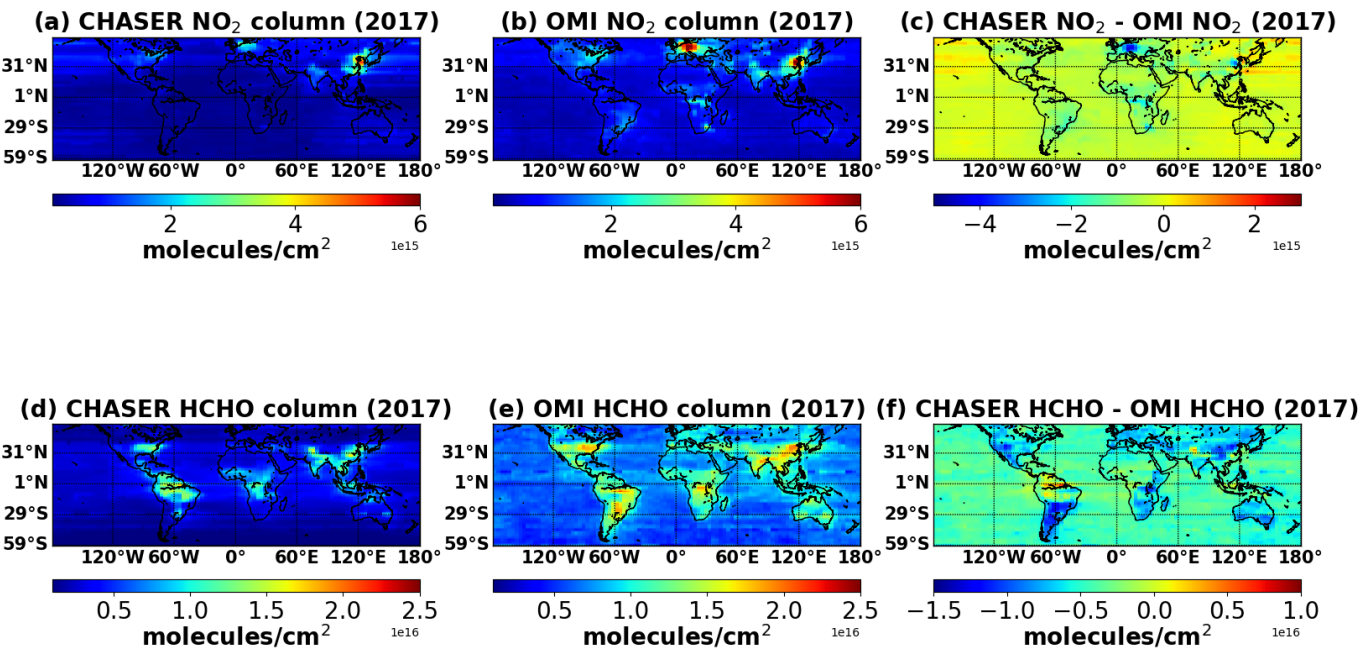
#### 3.2.1 Comparison between CHASER and OMI NO<sub>2</sub>

Figure 7 compares the simulated and observed annual mean tropospheric NO<sub>2</sub> columns. The statistics for the comparison are given in Table 5. The model captured the global spatial variation well with a spatial correlation ( $r$ ) of 0.70. The mean bias error (MBE) and the root mean square error (RMSE) are respectively,  $3 \times 10^{14}$  and  $5.4 \times 10^{14}$  molecules cm<sup>-2</sup>. On a global scale, CHASER estimations are negatively biased by 38% compared to OMI. Actually, studies evaluating global NO<sub>2</sub> simulations with satellite observations have reported similar negative biases (Miyazaki et al., 2012, Sekiya et al., 2018). The differences in the spatial representativeness between the model and observations is one potential reason for such negative biases. CHASER simulations at 1.1° improved the MBE and RMSE by 5 and 15%, respectively, compared to simulations at 2.8° (Sekiya et al. 2018). Moreover, Sekiya et al (2018) used NO<sub>2</sub> simulations with an updated inventory and compared the results with OMI observations from 2014. Although they reported a better global spatial correlation ( $r > 0.90$ ), the MBE ( $2.5 \times 10^{14}$  molecules cm<sup>-2</sup>) and RMSE ( $4.4 \times 10^{14}$  molecules cm<sup>-2</sup>) values at 2.8° resolution are comparable to those obtained from this study.

594 OMI retrievals show the highest NO<sub>2</sub> columns over eastern China (E-China) and Western Europe. Annual  
595 mean NO<sub>2</sub> columns over the remainder of the land areas are between  $7 \times 10^{14}$  and  $4 \times 10^{15}$  molecules cm<sup>-2</sup>.  
596 Over the land areas the differences between the datasets are mostly between  $-2 \times 10^{15}$  and  $5 \times 10^{14}$  molecules  
597 cm<sup>-2</sup>. Although CHASER also underestimates NO<sub>2</sub> columns over the ocean, the differences are lower than  
598 that of over lands. CHASER estimates are higher by  $\sim 5 \times 10^{14}$  molecules cm<sup>-2</sup> than OMI over Japan. Since  
599 2012, the NO<sub>2</sub> columns have shown a declining trend over Japan, mainly because of emission controls in  
600 China (Irie et al 2016). Probably because of simulations with an emission inventory earlier than 2012, the  
601 simulated values tend to be higher than observations.

602 Figure 8 compares the seasonal variations in the monthly mean NO<sub>2</sub> columns in some selected region.  
603 The error bars represent the 2-sigma standard deviation of the observed mean values. The numbers in  
604 each subplot signify the regional spatial correlation between the datasets. Over eastern China (E-China),  
605 CHASER values are negatively biased by 24%; the *r*-value is 0.68. The model captured the seasonality  
606 well within variation range of the observations. Over E- and W-USA (eastern and western USA), the  
607 respective *r*-values are 0.85 and 0.49 respectively. Simulated NO<sub>2</sub> columns are higher over E-USA than  
608 over W-USA, consistent with the observations. Although, in both regions model estimates are biased by  
609  $\sim 23\%$  in the lower side compared to OMI observations, the RMSE in E-USA are  $\sim 40\%$  higher than in W-  
610 USA.

611 Over Europe, CHASER estimates are negatively biased by 54%, with an *r*-value and RMSE of 0.80 and  
612  $1.28 \times 10^{15}$  molecules cm<sup>-2</sup>, respectively. The observed NO<sub>2</sub> levels over Europe are almost twice those of  
613 the W-USA. The model was unable to capture the regional differences. Model underestimations in Europe  
614 can be attributed to the older anthropogenic emission inventory used for the study. In fact, using the HTAP  
615 2010 inventory the MBE ( $-0.53 \times 10^{15}$  molecules cm<sup>-2</sup>) between OMI and CHASER NO<sub>2</sub> column  
616



618 **Figure 7:** (top panel) Annual mean tropospheric NO<sub>2</sub> ( $\times 10^{15}$  molecules cm<sup>-2</sup>) columns (a) simulated by CHASER  
619 and (b) retrieved from OMI observations. Limited NO<sub>2</sub> data in July and December met the filtering criteria, thus  
620 discarded from the calculation. (c) The differences between the simulated and observed NO<sub>2</sub> columns. (bottom  
621 panel) Annual mean HCHO ( $\times 10^{16}$  molecules cm<sup>-2</sup>) columns (d) simulated by CHASER and (e) retrieved from  
622 OMI observations. (f) The differences between the simulated and observed HCHO columns. The data for 2017 are  
623 plotted only. All the datasets are mapped onto a 2.8° bin grid.

624

625 simulations at 2.8 over Europe (Sekiya et al. 2018) was  $\sim 50\%$  lower than in the current study, although  
626 their RMSE value is similar.

627 Over India, MBE and RMSE for the annual mean NO<sub>2</sub> column are  $-4.3 \times 10^{14}$  and  $4.4 \times 10^{14}$  molecules  
628 cm<sup>-2</sup>, respectively, and the *r*-value is moderate (0.65). Although CHASER estimates are negatively biased  
629 by  
630  
631  
632 **Table 5:** Statistics of comparison of annual mean NO<sub>2</sub> and HCHO columns between CHASER and OMI. MBE1  
634 and MBE2 are the respective mean bias error. RMSE1 and RMSE2 are the respective root mean square errors. r1  
635 and r2 signifies the respective spatial correlation coefficient. The units of MBE1 and RMSE1 are  $\times 10^{15}$  molecules  
636 cm<sup>-2</sup>. MBE2 and RMSE2 values are in the unit of  $\times 10^{16}$  molecules cm<sup>-2</sup>.

Region	r1 (CHASER vs OMI NO <sub>2</sub> )	MBE1 (CHASER - OMI NO <sub>2</sub> )	RMSE1 (CHASER – OMI NO <sub>2</sub> )	r2 (CHASER vs OMI HCHO)	MBE2 (CHASER – OMI HCHO)	RMSE2 (CHASER – OMI HCHO)
Global	0.73	-0.30	0.54	0.74	- 0.45	0.49
E-China	0.68	-1.84	2.47	0.57	-0.63	0.64
E-USA	0.85	-0.62	0.63	0.91	-0.56	0.56
W-USA	0.49	-0.33	0.37	0.63	-0.71	0.71
Europe	0.80	-1.20	1.28	0.51	-0.67	0.68
India	0.65	-0.43	0.44	0.73	-0.56	0.57
N-Africa	0.58	-0.88	0.90	0.65	-0.29	0.32
S-Africa	0.80	-1.25	1.40	0.22	-0.66	0.70
S-America	0.87	-0.80	0.88	0.47	-0.31	0.40
SE Asia	0.57	-0.61	0.64	0.48	-0.41	0.44

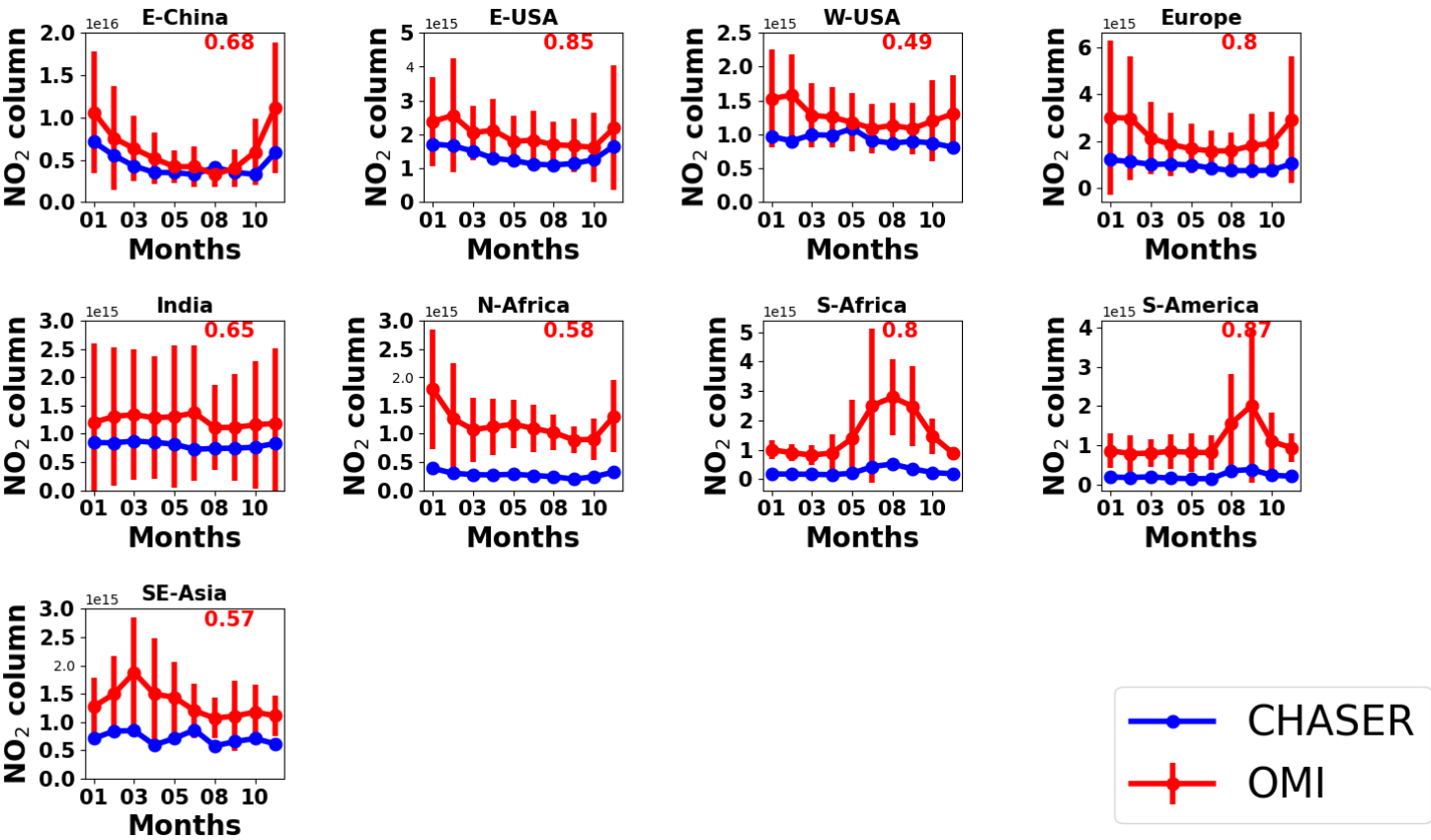
637  
638

639 32%, the values lie within the 2-sigma range of the observations. Sekiya et al. (2018) found no significant  
640 effect of higher model resolution on the MBE and RMSE in the Indian region.

641 Over N- and S-Africa (North and South Africa), the model values are biased low by more than 75%  
642 compared to the observations. Prominent biomass burning occurs in both regions, which explains the  
643 enhanced NO<sub>2</sub> levels in the OMI retrievals. High negative biases in the model values indicates that  
644 biomass burning NO<sub>x</sub> emissions for the African regions are likely underestimated. Similarly, CHASER  
645 underestimates NO<sub>2</sub> columns by 80% in South America, where pyrogenic emissions contributions are  
646 significant. CHASER estimates are lower than OMI in these regions, but model captured the spatial  
647 distribution well.

648 Over the SE-Asian (Southeast) region, OMI columns are enhanced during the dry season (i.e., January -  
649 April. Burning agricultural wastes is a common practice in many countries in Southeast Asia during the  
650 dry season, explaining the enhanced columns. The MBE ( $-6 \times 10^{14}$  molecules cm<sup>-2</sup>) and RMSE ( $6.4 \times$   
651  $10^{14}$  molecules cm<sup>-2</sup>) in the SE-Asia region are lower than the African regions (i.e., N-Africa, S-Africa,  
652 and S-America), where biomass burning is prominent.





654

655 **Figure 8:** Seasonal variations in tropospheric NO<sub>2</sub> columns in E-China (110° -123° E, 30° – 40° N), E-USA (32°  
656 – 43° N, 71° – 95° W), W-USA(32° – 43° N, 100° – 125° W), Europe (35° – 60° N, 0° – 30° E), India (7.5° – 54° N,  
657 68° – 97° E), N-Africa (5° – 15° N, 10° W – 30° E), S-Africa (5° -15° S, 10° -30° E), S-America (0° -20° S, 50° -  
658 70° W), and SE-Asia (10° – 20° N, 9° – 145° E). CHASER simulations and OMI retrievals are plotted in blue and  
659 red colors respectively. The error bars indicate the 2-sigma variation of the observed mean values. The number in  
660 the insets signifies the regional spatial correlation between CHASER and OMI NO<sub>2</sub> columns.

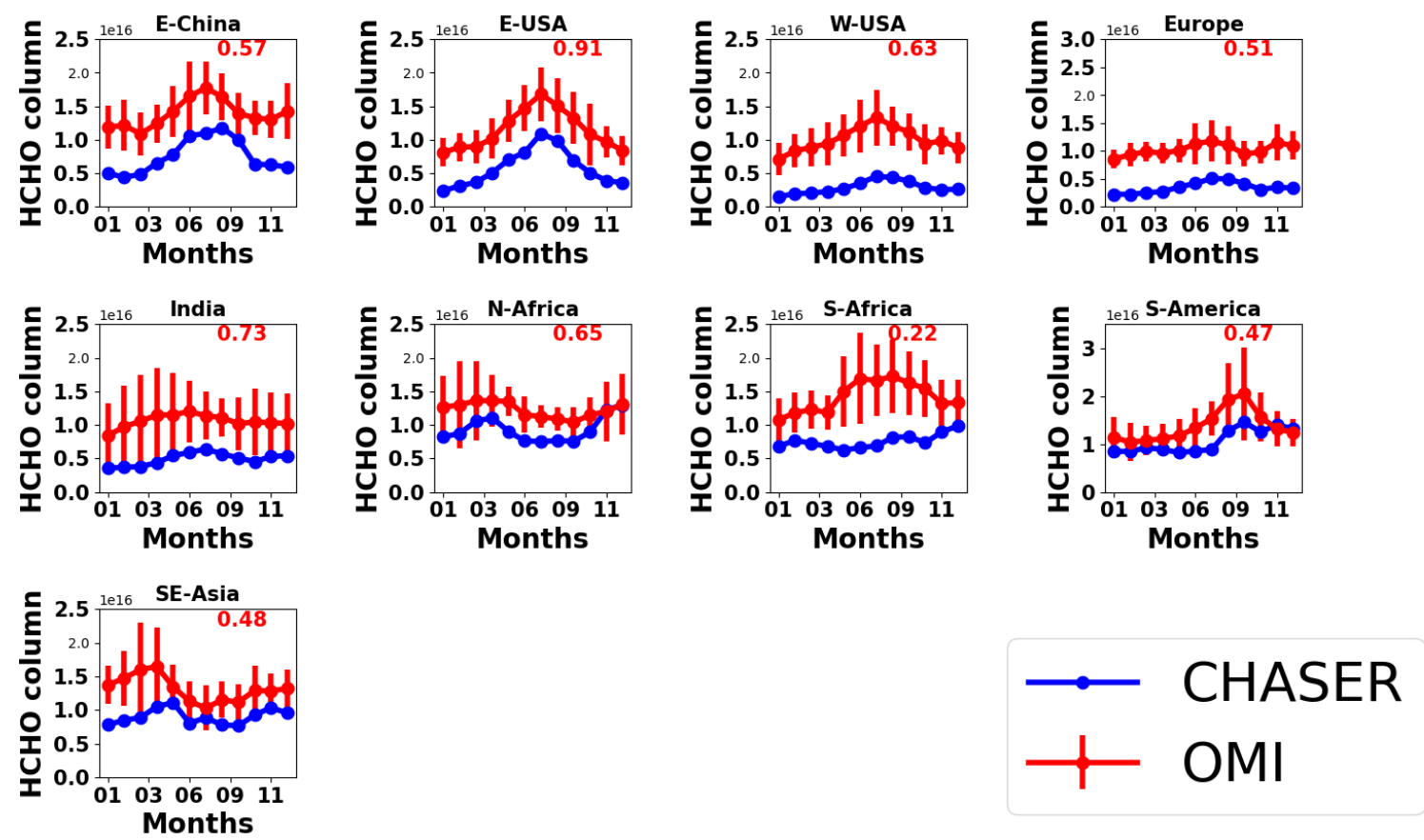
661

662 **3.2.2 Comparison between CHASER and OMI HCHO**

663 Figure 9 presents a comparison between the simulated and observed global annual mean HCHO columns.  
664 The statistics of the comparison are given in Table 5. CHASER is able to reproduce the observed global  
665 spatial variation well with  $r = 0.73$ . The global MBE and the RMSE are respectively,  $-4.5 \times 10^{15}$  and 4.9

666  $\times 10^{15}$  molecules  $\text{cm}^{-2}$ . MBE and RMSE for monthly mean fields show no distinctive seasonal variation  
 667 (Table S2). High HCHO columns are observed over China, Australia, Europe, India, Central Africa, South  
 668 America, and the United States. The model mostly underestimated the HCHO abundances in the higher  
 669 latitudes and Australia. Absolute differences between the model and observations in the higher latitudes  
 670 vary between  $5 \times 10^{15}$  and  $1 \times 10^{16}$  molecules  $\text{cm}^{-2}$ . Figure 9 compares the seasonal variations in the monthly  
 671 mean HCHO columns in some selected region. Therein error bars represent the 2-sigma standard  
 672 deviation of the observed mean values. The numbers in the respective subplots signify the regional spatial  
 673 correlation between the datasets.

674 Over E-China, CHASER HCHO estimates are negatively biased by 45% compared to OMI and the  $r$ -  
 675 value is greater than 0.50. The model reproduced the observed HCHO seasonality well including  
 676 enhanced peaks during the summer. The greatest differences between the datasets are observed during  
 677 the winter. Over E-USA, the spatial correlation between the datasets is greater than 0.90. Also, the  
 678 CHASER estimates are biased by 49% in the lower side. Simulations show that the peak in the HCHO  
 679 abundances occurs in July, which is consistent with the observations. The observed and simulated  
 680 magnitude of the seasonal modulation is 51 and 78%, respectively. The seasonality in the HCHO columns  
 681 in E-China and E-USA signifies a strong contribution from biogenic emissions. In both regions, the  
 682 observed peak HCHO column is  $\sim 1.75 \times 10^{16}$  molecules  $\text{cm}^{-2}$ . The simulated peak HCHO values are also  
 683 similar in both regions, despite the underestimation. Over W-USA and Europe, the negative biases in the  
 684 simulation are greater than 60%. However, the simulated peaks during summer are consistent with the  
 685 observations. The OMI retrievals show that the HCHO abundances in both regions are almost similar,  
 686 which has been well captured by CHASER, although the magnitude is underestimated.



689 **Figure 9:** Seasonal variations in HCHO columns in E-China (110° -123° E, 30° - 40° N), E-USA (32° - 43° N,  
690 71° - 95° W), W-USA(32° - 43° N, 100° - 125° W), Europe (35° - 60° N, 0° - 30° E), India (7.5° - 54° N, 68° -  
691 97° E), N-Africa (5° - 15° N, 10° W - 30° E), S-Africa (5° -15° S, 10° -30° E), S-America (0° -20° S, 50° -70° W),  
692 and SE-Asia (10° - 20° N, 9° - 145° E). CHASER simulations and OMI retrievals are plotted in blue and red colors  
693 respectively. The error bars indicate the 2-sigma variation of the observed mean values. The number in the insets  
694 signifies the regional spatial correlation between CHASER and OMI HCHO columns.

696 Over India, the model estimates mostly lie outside of the observational variation ranges, although,  
697 CHASER captured the spatial distribution well ( $r = 0.73$ ). Magnitudes of the seasonal variation in both  
698 OMI and CHASER are around 32%. Between the two African regions, CHASER demonstrated better  
699 capability for reproducing HCHO distribution in N-Africa ( $r = 0.65$ ). Negative model bias in N-Africa is

almost half (22%) that of S-Africa (46%). Observed N-African HCHO columns are mostly higher than  
 $1.2 \times 10^{16}$  molecules  $\text{cm}^{-2}$  during the biomass burning period (November - April). Although the modeled  
 values are lower than the observed values, the year-end columns (November - December) are similar.  
 Both datasets show low HCHO variation during May - September. Over the S-African region, the model  
 capabilities were limited.

Over S-America, the negative bias (~22%) in the model estimates compared to the observations is similar  
 to that of N-Africa. In addition to consistency in the year-end (November to December) columns,  
 CHASER well reproduced the biomass burning-led enhancements. The observed and simulated  
 magnitudes of seasonal modulation are 49 and 43%, respectively.

Over SE-Asia, CHASER reproduced the observed biomass burning-led enhanced HCHO columns during  
 the dry season (January - April), however, the occurrence of the peak is inconsistent. As discussed in  
 section 3.1, observed HCHO peaks related to biomass burning can vary depending on the fire numbers.  
 The  $r$ -value (0.48) is moderate and model is biased by 30% in the lower side. The model negative biases  
 in the biomass prone regions are lowest (<30%) among the discussed regions.

De Smedt et al. (2021) reported that cloud corrections can positively bias OMI HCHO columns up to  
 30% compared to Tropospheric Ozone Monitoring Instrument (TROPOMI) columns. Consequently,  
 uncertainties in the observations are also likely to contribute to the observed negative biases. Comparison  
 among CHASER, TROPOMI, and OMI HCHO columns is beyond the scope of this study. However, the  
 effects of uncertainties in the satellite retrievals on the negative biases is discussed qualitatively and  
 briefly. To demonstrate such effects, CHASER and TROPOMI HCHO columns for 2019 are compared  
 in Fig S3. The simulation settings and emission inventories are similar to those explained in section 3.2.3.  
 The comparison results are presented in Table S2. TROPOMI data has been processed following De  
 Smedt et al. (2021). The CHASER and TROPOMI HCHO spatial distribution correlates strongly with  $r$ -  
 value of 0.78. The values for MBE and RMSE are respectively,  $-2.3 \times 10^{15}$  and  $2.8 \times 10^{15}$  molecules  $\text{cm}^{-2}$ .  
 Compared to OMI and TROPOMI, CHASER HCHO columns are negatively biased, respectively, by  
 61 and 38%. The model biases are lower when compared to TROPOMI observations. Because of temporal  
 differences in the two comparisons, the biases cannot be compared quantitatively. However, the  
 differences in the biases signify that the observational uncertainties can strongly affect discrepancies

728 between the simulated and observed HCHO abundances. Moreover, using different cloud products may  
729 introduce inconsistencies in the OMI BIRA-IASB retrievals (De Smedt et al., 2021), affecting the  
730 comparison results. De Smedt et al. (2021) proposed to recalculate the OMI HCHO VCDs based on the  
731 AMF information to minimize cloud-induced uncertainties. Such a detailed method will be evaluated in  
732 our future studies.

733

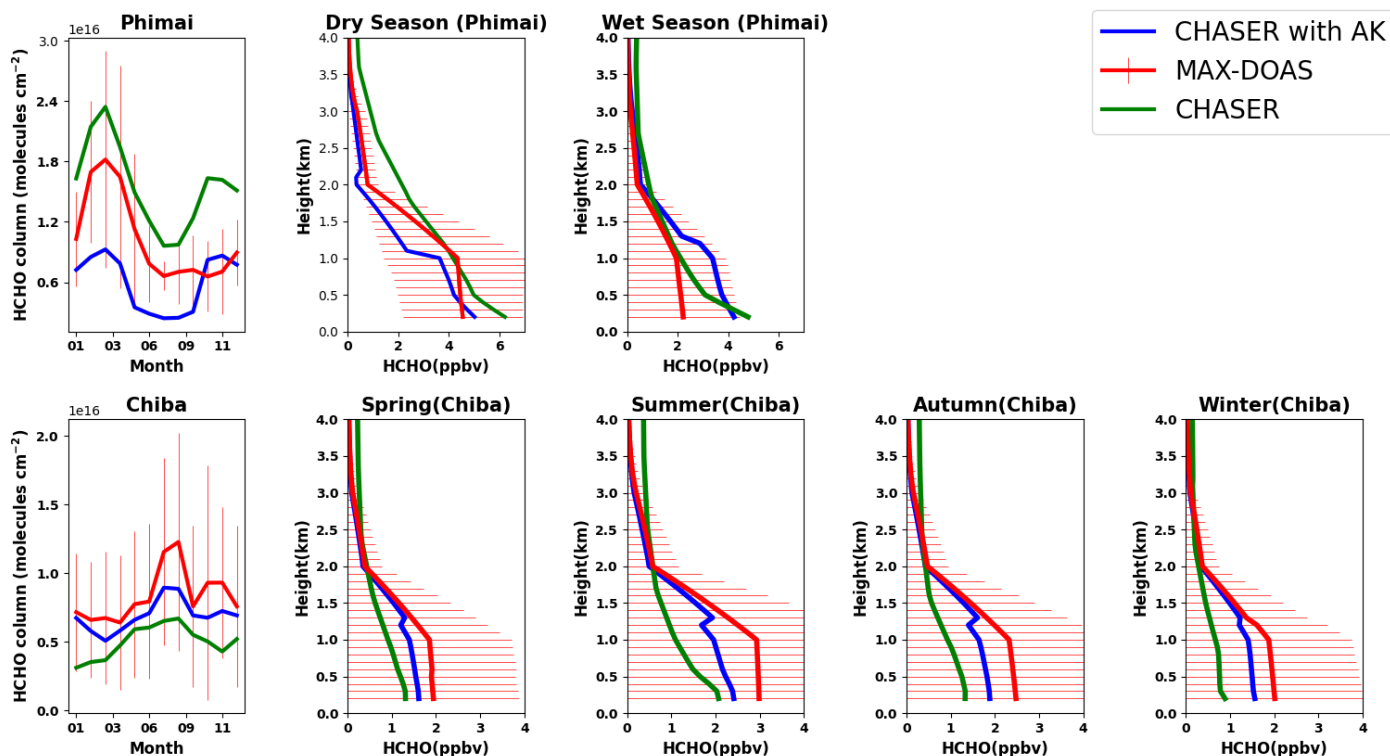
734

### 735 **3.3 Evaluation of CHASER simulations at the three sites**

#### 736 **3.3.1 Evaluation of CHASER HCHO at Phimai and Chiba**

737 The seasonally averaged observed and modeled HCHO profiles and partial columns in the 0 - 4 km  
738 altitude range at Phimai and Chiba are presented in Fig. 10. The CHASER outputs smoothed with MAX-  
739 DOAS averaging kernels (AK) are also depicted. The AK is applied following Franco et al. (2015). First,  
740 the CHASER HCHO profiles are interpolated to the MAX-DOAS vertical grids. Next, the MAX-DOAS  
741 AK information from individual retrieved profiles is seasonally averaged according to the climate  
742 classifications of each site. Finally, the CHASER outputs on the coincident days are selected, and the  
743 seasonally averaged AK is applied to the daily mean interpolated profile. Applying individual AKs to the  
744 model outputs yielded similar results. The seasonally averaged AKs for both sites are shown in Fig S4.  
745 The coincident days at Phimai and Chiba were respectively, 690 and 668.

746 At Phimai, CHASER predicted the increase in the HCHO partial columns during the dry season and  
747 well-reproduced the HCHO seasonality. The simulated and observed seasonality correlates strongly with  
748  $R$ -value of 0.96. The modeled monthly mean values during the dry season are found to be within the  $1\sigma$   
749 standard deviation of the observed values, indicating that the pyrogenic emissions estimates used for the  
750 simulations are reasonable. CHASER predicted a 41% increase in the HCHO column during January -  
751 March, consistent with the observations (41%). CHASER overestimates the HCHO columns in both  
752 seasons, and the mean bias error (MBE) (CHASER – MAX-DOAS) is lower ( $3.7 \times 10^{15}$  molecules  $\text{cm}^{-2}$ )  
753 (Table 6) during the wet season. Although underestimated, the dry season smoothed column values are  
754 within the  $1\sigma$  range.



755 **Figure 10.** Seasonal variations in the HCHO partial columns at 0 - 4 km and vertical profiles during all seasons at  
 756 Phimai and Chiba, as inferred from the MAX-DOAS observations (red) and CHASER simulation (green). The  
 757 CHASER HCHO partial column and vertical profile smoothed with the MAX-DOAS AK are coloured blue. The  
 758 AK information of all the screened (as explained in section 2.2) retrievals were averaged based on the seasonal  
 759 classification of the respective sites. The coincident time and date between the model and observations are selected  
 760 only. Error bars indicate the one sigma standard deviation of mean values of the MAX-DOAS observations.

761  
 762 The modeled and observed HCHO mixing ratios in the 1- 2km layers during the wet season are almost  
 763 identical, whereas VMR near the surface (i.e., 0 - 1 km) differ by 30%. The absolute mean difference in  
 764 the 0-4 km layer is ~0.45ppbv, with the maximum difference of 2.58 ppbv below 200 m. CHASER has  
 765 demonstrated good capabilities for reproducing the HCHO profile in the 0.5 – 4 km layer during the wet  
 766 season. The significance of AK information is low for the wet season. However, smoothing the model  
 767 profiles reduces the overall MBE by 43%.

768

**Table 6:** Comparison of the seasonal mean HCHO partial columns and profiles (0-4 km) between MAX-DOAS and CHASER at Phimai and Chiba. MBE (CHASER – MAX-DOAS) is the mean bias error. The partial column and profile MBE units are respectively,  $\times 10^{16}$  molecules  $\text{cm}^{-2}$  and ppbv, respectively.

Site	Season	Partial column MBE	Smoothed Partial column MBE	Profile MBE	Smoothed Profile MBE
Phimai	Overall	0.28	-0.07	0.35	0.01
Phimai	Dry	0.37	-0.28	0.58	-0.38
Phimai	Wet	0.21	0.07	0.45	0.33
Chiba	Overall	-0.12	-0.05	-0.37	-0.11
Chiba	Spring	-0.07	-0.04	-0.22	-0.12
Chiba	Summer	-0.16	-0.08	-0.45	-0.26
Chiba	Autumn	-0.10	-0.04	-0.40	-0.19
Chiba	Winter	-0.09	-0.01	-0.42	0.11

During the dry season, the respective absolute mean and maximum difference in the datasets in the 0 -1 km layers is ~1 and ~2ppbv. The observed and simulated seasonal differences in the 0-1 km are 50 and 34%, respectively. Simulated dry season profile values at the heights greater than ~2 km is out of the  $1\sigma$  variation range. The two-potential reasons for such differences are lower measurement sensitivity in the free troposphere and the overestimated Southeast Asian biogenic emissions in the model. Despite the measurement limitations, CHASER and MAX-DOAS wet season profiles up to 3 km are consistent. Consequently, it is likely that the biogenic emissions for this region in the model are overestimated. The Southeast Asian isoprene emissions in CHASER is  $128 \text{ Tgyr}^{-1}$ , higher than the CMAS-GLO-BIO (Sindelarova et al., 2022) inventory ( $78 \text{ Tgyr}^{-1}$ ). However, the dry season HCHO profiles in 0 - 2 km are well simulated. Smoothing underestimates the dry season profile within the  $1\sigma$  variation range but improved simulations below 200 m. At heights greater than 3 km, the smoothed values mostly reproduce the a priori because of reduced measurement sensitivity (i.e., low AK value, indicating limited information was retrievable).

788 Moderate correlation ( $R=0.58$ ) can be observed between the modeled and observed HCHO partial  
789 columns at Chiba. CHASER was able to reproduce the peak in the partial columns in August. The model  
790 predicts a 41% increase in the HCHO columns during January - August, whereas the observed increase  
791 is 54%. Although Chiba is an urban site, the HCHO and temperature seasonal variations show a tight  
792 correlation ( $R\sim 0.70$ ) (Fig S5), suggesting that changes in biogenic emissions modulate HCHO  
793 seasonality. Similarly, the modeled seasonality is consistent with temperature variation (Fig. S4). Thus,  
794 the simulated HCHO seasonality in Chiba is reasonable, despite underestimation of absolute values.  
795 Smoothing the simulations improve the correlation, and the MBE is reduced by 54% (Table 6).

796 The CHASER HCHO profiles in the 0 - 4 km layers are lower than the observations, with an MBE  
797 of 0.39 ppbv. The absolute differences in the modeled and retrieved HCHO profiles in the 0-2 km layer  
798 during all seasons are higher than at Phimai. Absolute mean differences of  $\sim 1$  ppbv and higher are mainly  
799 observed for 0 to 2 km. In addition, the vertical gradients of the simulated profiles are low compared to  
800 those at Phimai. The modeled profiles at Chiba resemble the HCHO profiles measured over the ocean  
801 during the INTEx-B (Intercontinental Chemical Transport Experiment: Phase B) (Boeke et al., 2011).  
802 The Chiba site is near the sea, and coarse CHASER resolution includes the ocean pixels. Moreover, urban  
803 surfaces are not homogeneous. Thus, a significant part of the profile discrepancies is likely related to the  
804 systematic differences, in addition to emission estimates. However, the model estimates lie within the  
805 standard deviation range of the measurements. Because of the low gradients in the simulated profiles, the  
806 smoothed profiles mostly imitated the a priori values even below 2 km. Overall, given the large  
807 uncertainty on the MAX-DOAS profiles (Fig. 10), the differences between the observations and smoothed  
808 profile are statistically insignificant. Effects of the horizontal resolution on the simulated HCHO levels is  
809 discussed in section 3.3.4.

810

811

### 812 **3.3.2 Evaluation of CHASER NO<sub>2</sub> in Phimai and Chiba**

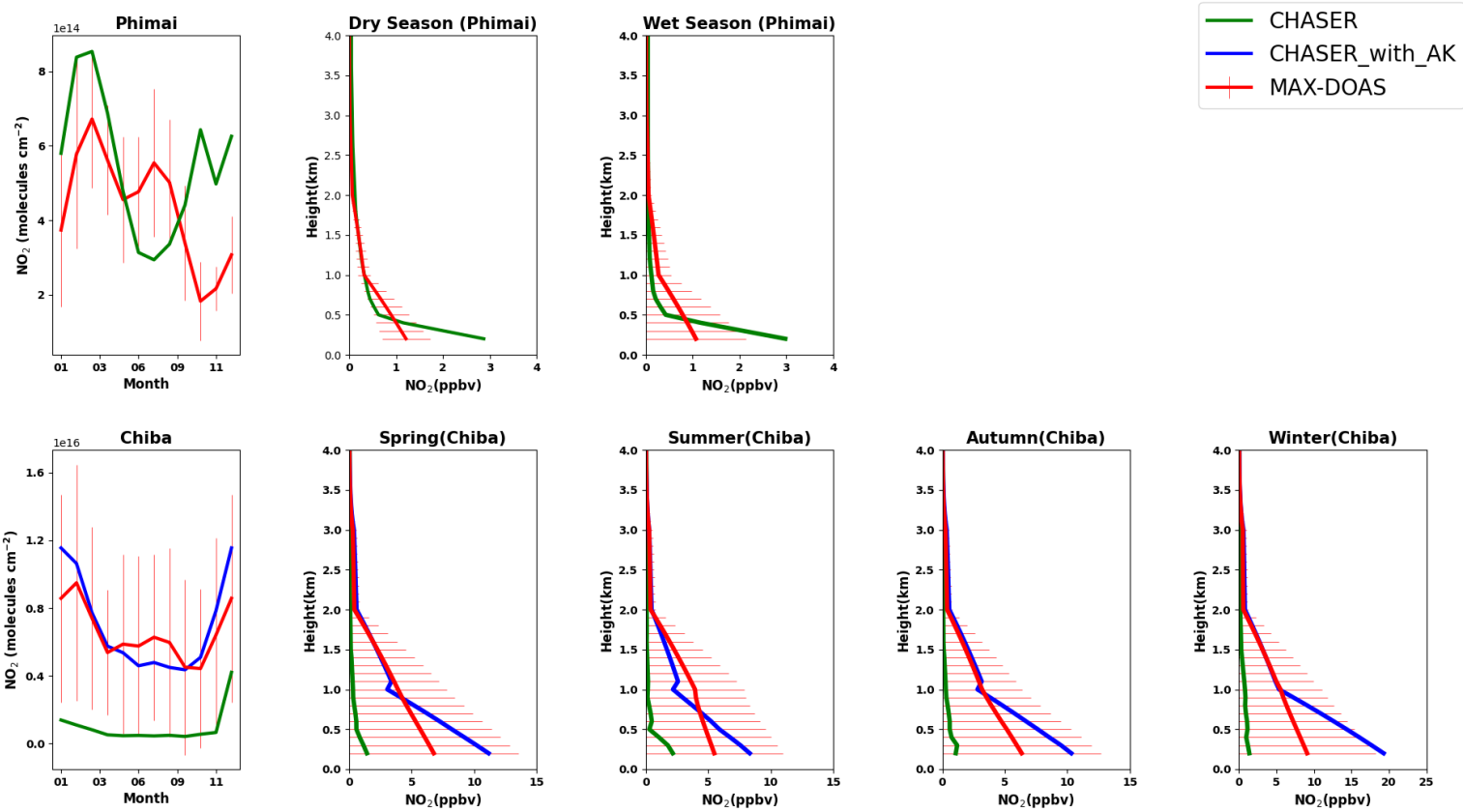
813 Figure 11 presents the seasonal averages of the MAX-DOAS and CHASER NO<sub>2</sub> profiles and partial  
814 columns (0 - 4 km) at Phimai and Chiba. The AK is applied to the modeled outputs for the Chiba site  
815 only.



816 Figure S5 of the supplementary information presents a comparison of the observations, model, and  
817 smoothed model profiles averaged within the 0 - 2 km layer at Phimai. Smoothing with different a priori  
818 values is depicted to demonstrate the effects of the a priori values. The smoothed NO<sub>2</sub> concentrations,  
819 calculated using the original a priori values, show a seasonal variation shift. The mean smoothed profile  
820 resembles the observations when a priori values are reduced by 50%; however, the dry season values are  
821 similar in both cases. Two test cases of smoothing profiles using apriori values above 500 and 800 m  
822 shows good agreement with the observations; however, the results are sensitive to the apriori values.  
823 Because smoothed profiles are strongly biased to the apriori choice, the smoothing results obtained for  
824 the Phimai site are discarded.

825 The modeled NO<sub>2</sub> partial column at Phimai shows good agreement with observations made during the  
826 dry season. CHASER well reproduces the enhanced NO<sub>2</sub> columns attributable to biomass burning within  
827 the standard deviation of the observations. The peak in the NO<sub>2</sub> levels during March is consistent in both  
828 datasets. Although the seasonality does not agree in other months, the overall MBE is  $8 \times 10^{13}$  molecule  
829 cm<sup>-2</sup> (Table 7). Above 500 m, the datasets shows excellent agreement. The absolute mean differences in  
830 the 0 - 1km layer are 0.22 ppbv, and the maximum difference of ~1.9 ppbv is observed near the surface.  
831 Amidst the biomass burning influence, the NO<sub>2</sub> concentrations at Phimai are mostly < 1 ppbv. Thus, the  
832 results of comparisons demonstrate CHASER's good capabilities in regions characterized by low NO<sub>2</sub>  
833 concentrations. Moreover, when NO<sub>2</sub> concentrations are less than < 1 ppbv, the AK information seems  
834 less significant if the model can capture low-concentration scenarios.

835



838 **Figure 11.** Seasonal variation in NO<sub>2</sub> partial columns from 0 - 4 km and vertical profiles during all seasons at  
839 Phimai and Chiba, as inferred from the MAX-DOAS observations (red) and CHASER simulation(green). The  
840 CHASER NO<sub>2</sub> partial column and vertical profile smoothed with the MAX-DOAS AK are coloured in blue. The  
841 coincident time and date between the model and observations are selected only. The error bars represent the one  
842 sigma standard deviation of mean values of the MAX-DOAS observations.

**Table 7:** Comparison of the seasonal mean NO<sub>2</sub> partial columns and profiles (0-4 km) between MAX-DOAS and CHASER at Phimai and Chiba. MBE (CHASER – MAX-DOAS) is the mean bias error. The partial column and profile MBE units are  $\times 10^{15}$  molecules cm<sup>-2</sup> and ppbv, respectively.

Site	Season	Partial column MBE	Smoothed Partial column MBE	Profile MBE	Smoothed Profile MBE
Phimai	Overall	0.08		0.11	
Phimai	Dry	0.18		0.09	
Phimai	Wet	-0.14		0.02	
Chiba	Overall	-5.58	-1.90	-3.27	-1.66
Chiba	Spring	-5.56	-2.00	-3.19	-1.74
Chiba	Summer	-5.52	-2.87	-2.85	-1.86
Chiba	Autumn	-4.57	-1.24	-2.74	-1.40
Chiba	Winter	-6.64	-1.50	-4.30	-1.63

Although the datasets are moderately correlated ( $R=0.59$ ) at Chiba, the model largely underestimates the NO<sub>2</sub> partial column with MBE of  $\sim 5 \times 10^{15}$  molecules cm<sup>-2</sup>. The model predicts almost constant NO<sub>2</sub> profiles and columns throughout the year. Therefore, the respective seasonal biases are almost similar. The vertical gradient of the modeled NO<sub>2</sub> profiles is also low, too, similarly to the HCHO profiles. The model resolution can be a potential cause for such significant underestimation. The AKs improved the partial column and profiles significantly, reducing the MBE by more than 50%. However, the smoothed profiles and partial columns between the 0 - 2 km layer, differ significantly from the simulations, suggesting that the a priori values strongly affect the smoothed profiles. Consequently, the smoothed NO<sub>2</sub> profiles at Chiba (Fig.S7) are biased to the a priori values, similar to that of Phimai (Fig. S6). NO<sub>2</sub> smoothed profile sensitivity to a priori values might be attributable to our retrieval procedure. The a priori data are taken from the measured SCD and retrieved VCD values. As a result, the values are sensitive in the 0 - 2 km layer, similarly to the observations. Using a priori values other than those obtained from observations can affect such sensitivity. The smoothing sensitivity to a priori values is stronger for NO<sub>2</sub> than HCHO. The NO<sub>2</sub> profile gradient is higher than that of HCHO (Figs. 10 and 11), which means that,

866 within 10 km (MAX-DOAS horizontal resolution), the NO<sub>2</sub> mixing ratio and a priori variability (sources  
867 and sinks) is higher than those of HCHO, leading to a stronger a priori effect on the smoothed profiles.  
868

869 The mean NO<sub>2</sub> mixing ratios in the 0 - 2 km layer in 2018, simulated at spatial resolutions of  $2.8^{\circ} \times 2.8^{\circ}$   
870 (standard) and  $1.4^{\circ} \times 1.4^{\circ}$ , are compared with observations at Chiba, as depicted in Fig.12. The error bars  
871 are the  $1\sigma$  standard deviation of the observations. Higher resolution simulations reduced the overall MBE  
872 by 35% (Table 8). NO<sub>2</sub> concentrations at  $1.4^{\circ}$  are now within the variation range of the observations. The  
873  $1.4^{\circ}$  simulation captured the NO<sub>2</sub> seasonal variability better than at  $2.8^{\circ}$ . Despite improved resolution, the  
874 model values are underestimated, with the highest MBE during the winter. According to Miyazaki et al.  
875 (2020), the seasonality in the anthropogenic emissions, primarily wintertime heating, is not well  
876 represented in the emission inventories, which could likely underestimate winter NO<sub>2</sub> levels. The best  
877 agreement between the datasets is observed during summer and spring, with an MBE of ~1 ppbv on a  
878 seasonal scale.  
879

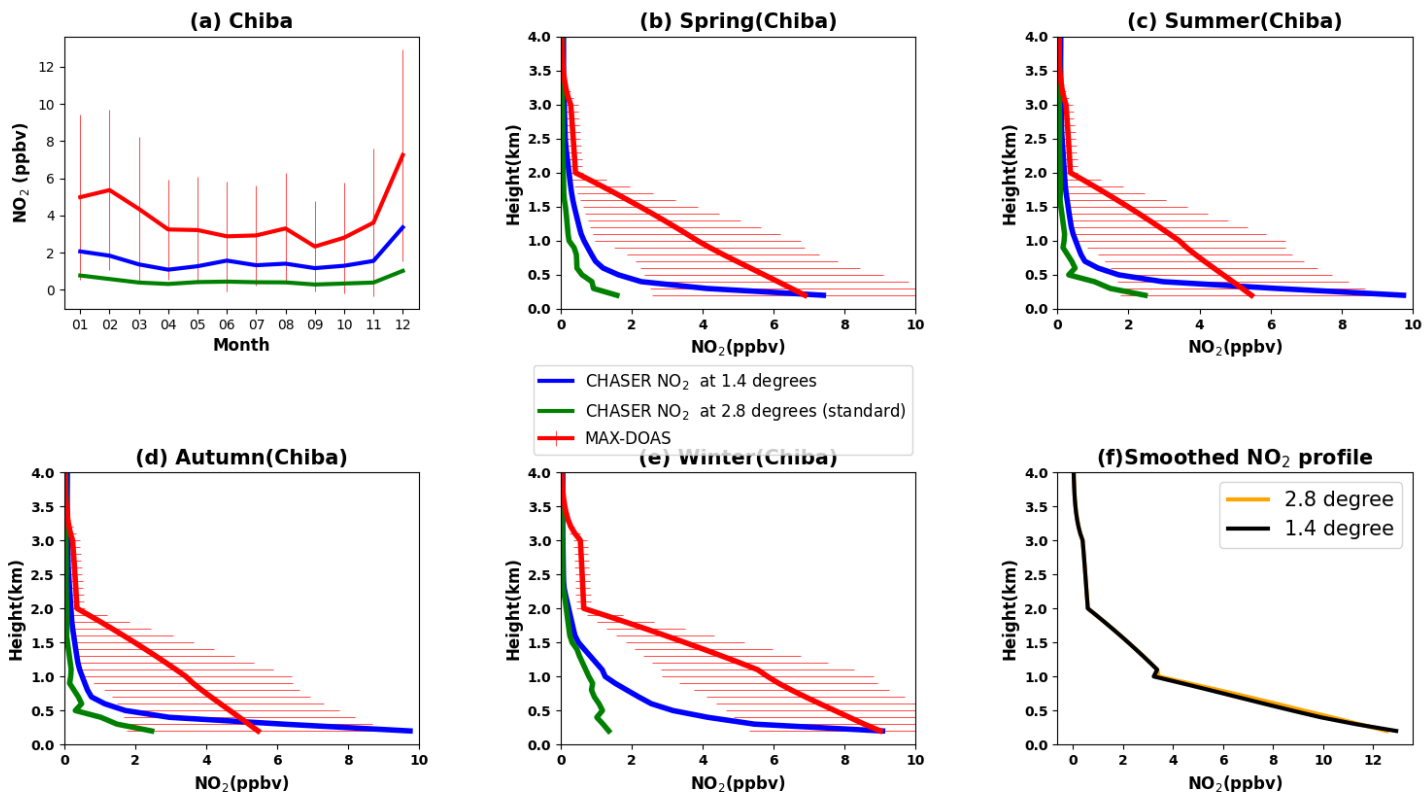


**Figure 12:** (a) Seasonal variations in the NO<sub>2</sub> mixing ratios in the 0 - 2 km layer at Chiba, as inferred from the MAX-DOAS observations (red) and two CHASER simulations at 2.8°(green) and 1.4°(blue) resolutions. The simulated NO<sub>2</sub> profiles at 2.8°(green) and 1.4°(blue) resolutions during (b) spring, (c) summer, (d) autumn, and (e) winter are shown with the observed seasonal profiles at Chiba. Only data (both observed and simulated) for 2018 are plotted. The coincident time and date between the model and observations are selected only. The error bars in (a), (b), (c), and (d) represent the one sigma standard deviation of mean values of the MAX-DOAS observations.

NO<sub>2</sub> profiles at 2.8° and 1.4° resolution are shown in Figs. 12(b - e). A strong effect of the increased resolution is observed below 500 m, reducing the negative bias by 70% near the surface. Above 500 m, the effects of higher resolution are limited, with an MBE reduction of 12% in the 0.6 – 2 km. Although the near-surface NO<sub>2</sub> concentrations at 1.4° resolution are overestimated, the values are within the standard deviation of the observations. At around 200m, winter mean NO<sub>2</sub> concentrations at 1.4°

893 resolution are identical to the observations (~9 ppbv), and the summer mean is overestimated. Moreover,  
894 the NO<sub>2</sub> levels above 2 km are similar at both resolutions. The resolution effects on NO<sub>2</sub> profiles vary  
895 with the location and season (Williams et al., 2017). For example, CHASER NO<sub>2</sub> at 1.1° resolution  
896 improved the agreement with aircraft observations below 650 hPa significantly over the Denver  
897 metropolitan area (Sekiya et al. 2018), whereas, at Chiba, the 1.4° resolution improved the surface  
898 estimates. Consequently, the horizontal resolution is not the only reason for the model underestimation.  
899 Other factors such as the vertical resolution, uncertainties in emission inventories, and chemical kinetics,  
900 can also affect the simulated NO<sub>2</sub> estimates. Effects of the emission inventory is discussed in section  
901 3.3.4.

902 Figure 12(f) shows the smoothed NO<sub>2</sub> profiles at both resolutions. Although the profile shapes are  
903 different, the smoothed profiles are almost identical, which demonstrates that, smoothed NO<sub>2</sub> profile  
904 sensitivity to a priori choice is mostly independent of the model resolution.

905

906 **Table 8:** Comparison of the seasonal mean NO<sub>2</sub> profiles (0-2 km) among MAX-DOAS and CHASER simulations  
907 at 2.8° and 1.4° resolutions at Chiba. MBE at (CHASER – MAX-DOAS) 1.4° and 2.8° are the mean bias error at  
908 the respective resolutions. The MBE unit is ppbv.

Season	MBE at 1.4°	MBE at 2.8°
Overall	-2.24	-3.37
Spring	-2.26	-3.23
Summer	-1.50	-2.47
Autumn	-1.57	-2.57
Winter	-3.44	-5.07

909

910

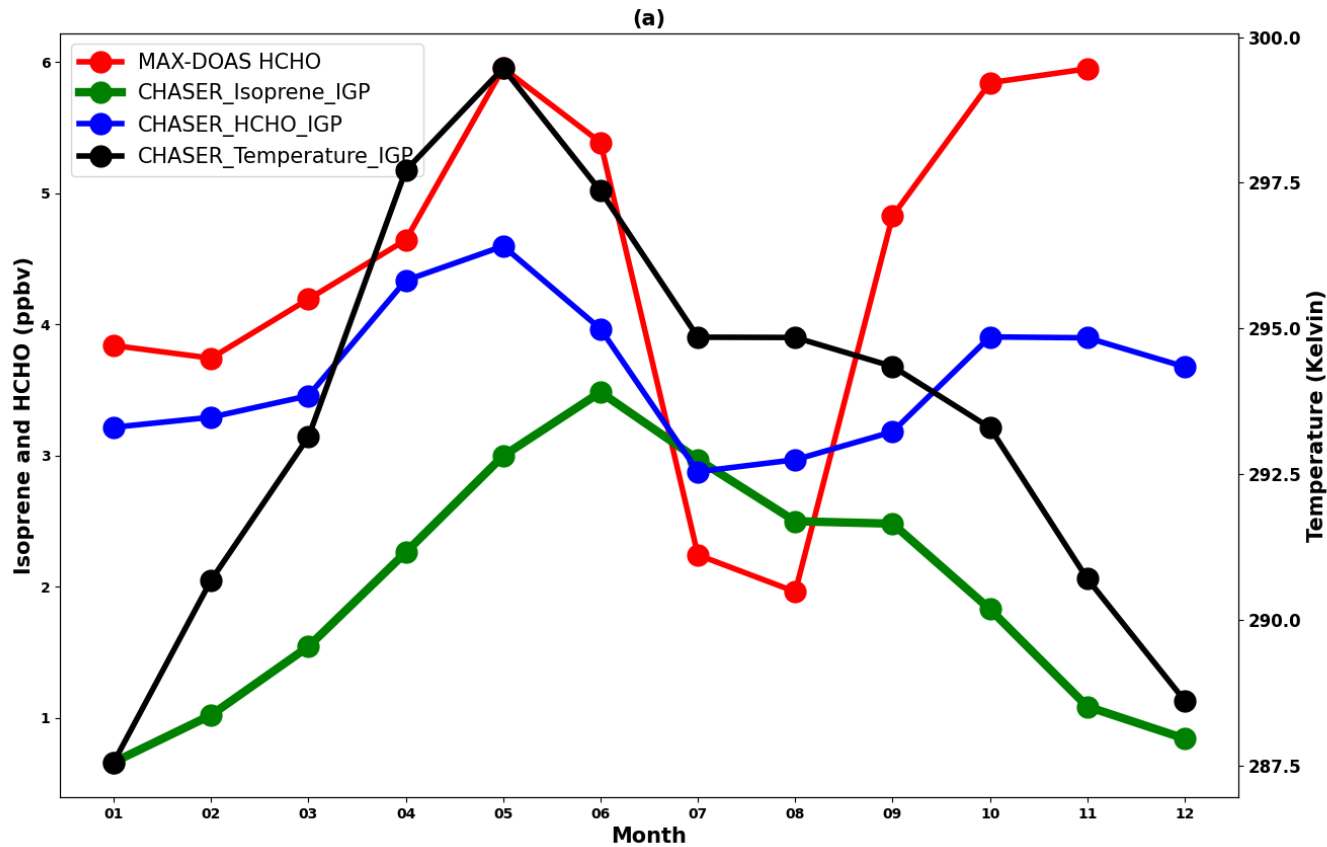
911

912

913

914 **3.3.3 Evaluation of CHASER HCHO in the IGP region**

915 The IGP is the most fertile region in South Asia, which accounts for approximately 50% of the total  
916 agricultural production of India and is one of the significant contributing regions to the global greening  
917 based on leaf area index (Sarmah et al., 2021). Moreover, IGP is one of the regional HCHO hotspots in  
918 India (Chutia et al., 2019). The observed HCHO seasonality at Pantnagar is consistent with that reported  
919 by Mahajan et al. (2015) for the entire IGP region. Consequently, comparison with the HCHO retrievals  
920 in Pantnagar can assess the model capability in the IGP region. The spatial representiveness is a  
921 limitation for comparison between a point measurement and regional simulations. Thus, the results are  
922 interpreted qualitatively. Because of the availability of a dataset with continuous observations, only the  
923 comparison for 2017 is shown in Fig. 13.



924

925 **Figure 13.** Seasonal variations in the MAX-DOAS (red) and CHASER (blue) HCHO concentrations at Pantnagar  
926 and the IGP region, respectively, in 2017. The coincident dates between the observations and model are plotted

only. The CHASER simulated isoprene and temperature seasonality are shown respectively, in green and black colours. Only the daytime simulated values were considered for the plot.

The modeled HCHO seasonal variations in the IGP region correlate well with the observations at Pantnagar ( $R \sim 0.80$ ). The enhancement in the HCHO concentrations during the spring and post-monsoon season is well reproduced by CHASER, which indicates that CHASER can capture HCHO variation in complex terrain region such as IGP. Figure 13 also depicts the isoprene concentrations and temperature in the IGP region, in addition to the HCHO concentrations. Oxidization of precursor hydrocarbons and photochemical reactions are the most dominant sources of HCHO. Also, isoprene is the most abundant hydrocarbon in the atmosphere. The average ambient isoprene concentrations during July, August, and September in the IGP region are  $1.4 \pm 0.3$  ppbv (Mishra et al., 2020). Therefore, the CHASER isoprene concentration range of  $1.5 - 2$  ppbv during the monsoon season seems reasonable. The HCHO concentrations in the IGP region reach a peak during the spring and post-monsoon seasons. A strong correlation between HCHO, isoprene, and temperature variation ( $R \sim 0.90$ ) during the first half of the year indicates that the change in biogenic emissions strongly drives the HCHO seasonal modulation. The observed enhancement in the HCHO levels during spring at Pantnagar is related to biomass burning. The biomass burning events are primarily concentrated in the northwest IGP region (Kumar and Sinha, 2021), where the site is located. On a regional scale, the biomass burning effects is expected to smear. Thus, the strong effect of the biogenic emission on the regional HCHO modulation is reasonable. HCHO modulation differs from isoprene and temperature during the post-monsoon period, suggesting a greater role of biomass burning and anthropogenic emissions. Consequently, the physical processes driving the HCHO seasonality in the IGP region are well reflected in the CHASER simulations.

### 3.3.4 Effects of the model resolution and emission inventories on results

Effects of the spatial resolution on the evaluation results is assessed by comparing the results of CHASER simulations at  $2.8^\circ$  and  $1.4^\circ$  resolutions with the surface observations, as shown in Fig. 14. Only, the simulated surface HCHO and  $\text{NO}_2$  concentrations during 2017 are shown only. The statistics are provided in Table 9. For the Pantnagar site, only the simulations are presented. At Phimai, the HCHO simulations



differ by 3%. The standard simulation shows better agreement with the observations. The higher MBE at 1.4° occurred mostly because of the model overestimation during the wet season. The NO<sub>2</sub> mixing ratios at the two resolution differ by 9%. The MBEs for both trace gases at Phimai are less than 1 ppbv. Thus, the HCHO and NO<sub>2</sub> standard simulations at 2.8° can be regarded as reasonable for regions characterized by low NO<sub>2</sub> levels (<1 ppbv). At Chiba, surface NO<sub>2</sub> and HCHO mixing ratios at 1.4° resolution differ respectively, by 61 and 19%. The NO<sub>2</sub> MBE at 1.4° resolution improved significantly, indicating a strong effect of the model resolution. However, discussion in section 3.2.2 showed limited resolution-based improvement in the overall profile. Results for MBE in the HCHO mixing ratios at 1.4° mostly improved during summer. The wintertime HCHO estimates at both resolutions are similar. In contrast to Chiba and Phimai, differences in the HCHO simulations (30%) at Pantnagar are greater than those of NO<sub>2</sub> (3%). The effect of model resolution varying with location and season was also reported by Sekiya et al. (2018). Compared to the other two sites, differences in the NO<sub>2</sub> simulations at Chiba are larger. This finding is consistent with the results by William et al (2017), which found larger differences with changing model resolution over urban areas.

Although the NO<sub>x</sub> estimates for the low NO<sub>2</sub> regions seem reasonable, global NO<sub>x</sub> emissions have changed since 2008(i.e., EDGAR-HTAP (2008) emissions used for this study). A recent study by Miyazaki et al. (2020) reported changes in global NO<sub>x</sub> emissions from 2005 to 2018. They found a continuous 30% increase in NO<sub>x</sub> emissions in India since 2005. REAS v3 (Regional Emission inventory in Asia version 3) inventory estimated a 23% increase in NO<sub>x</sub> emissions in India between 2010 - 2015, and power plants were the most significant contributor. Many power plants are clustered along the IGP region (Nair et al., 2007). Thus, the current simulation settings are likely to underestimate the NO<sub>2</sub> mixing ratios and columns in the IGP region. Figure S8 presents comparison of CHASER and OMI NO<sub>2</sub> columns for 2017 over the IGP region. Although the modeled columns are biased by 32% in the lower side, the spatial correlation between the datasets is high ( $r=0.78$ ). CHASER values lie within the range of variation of the observations. Although underestimated, NO<sub>2</sub> estimates in the IGP based on the current inventory are yet reasonable. Sekiya et al., (2018) used higher model resolution and updated emission inventory (HTAP 2010 for simulations in 2014) and reported ~30% lower MBE over India. However, the RMSE values of both studies are comparable.

983 NO<sub>x</sub> emissions in Japan have shown continuous decline since the execution of pollution control policies  
984 in 1970 (Ohara et al., 2020). Irie et al. (2021) reported a declining trend in NO<sub>2</sub> levels in Chiba since  
985 2012, echoing results obtained by Miyazaki et al. (2020) throughout Japan. The bias between CHASER  
986 and OMI NO<sub>2</sub> column over Japan is non-significant (Fig. S8 and Table S3). Thus, an updated inventory  
987 will not substantially affect the comparison results at the Chiba site. NO<sub>x</sub> emissions increased  
988 considerably in Southeast Asia. CHASER NO<sub>2</sub> estimates for Thailand based on HTAP 2008 inventory  
989 are biased by 45% in the lower side compared to OMI (Fig. S8). However, Phimai being a rural site, the  
990 NO<sub>x</sub> levels are expected to be low. Changes in biomass burning NO<sub>x</sub> estimates are likely to affect the  
991 model estimates. Because, the NO<sub>2</sub> levels at Phimai are mostly less than 1 ppbv, the effect of updated  
992 inventory on the comparison results is expected to be minimal.

993 CHASER HCHO columns over Japan, the IGP region, and Thailand are negatively biased respectively,  
994 by 60, 36, and 32% compared to OMI observations, with *r*-values of 0.5 – 0.7 (Fig. S8). Surl et al. (2018)  
995 reported spatial correlation of ~0.5 between GEOS-CHEM and OMI over the IGP region. Anthropogenic  
996 VOC emissions in India and other Asian cities have increased since 2005, whereas a negative trend has  
997 been observed over Japan (Bauwens et al., 2022). The REAS inventory estimated a 5% increase in  
998 NMVOCs in India since 2005. Moreover, anthropogenic emission contributes strongly to the HCHO  
999 abundances in the IGP region (Kumar and Sinha 2021). Thus, updated anthropogenic VOC emission  
1000 inventory is likely to improve the model HCHO estimates in the study regions. However, the formation  
1001 pathway of HCHO from isoprene emissions is a non-linear function of NO<sub>x</sub> chemistry. Consequently, the  
1002 effects of NO<sub>x</sub> emissions changes on the overall HCHO simulations cannot be assessed based on current  
1003 analyses explained herein.

1004

CHASER simulations at 2.8 degree  
 CHASER simulations at 1.4 degree  
 MAX-DOAS

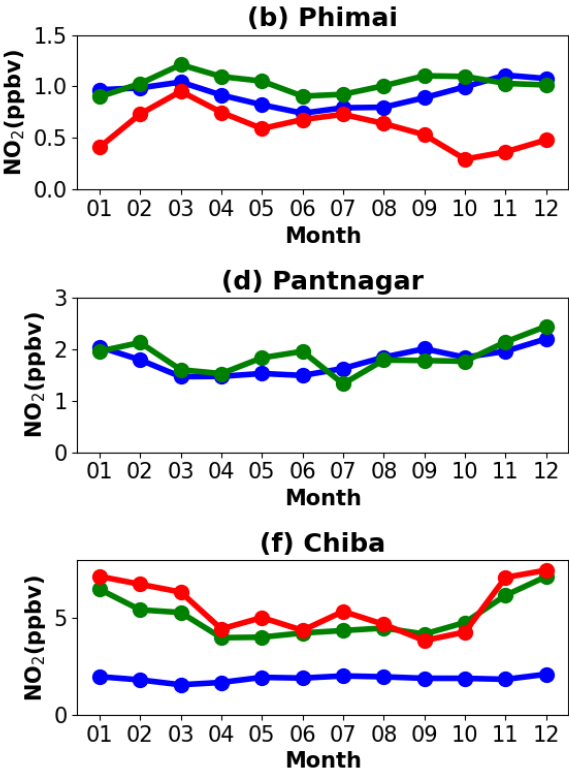
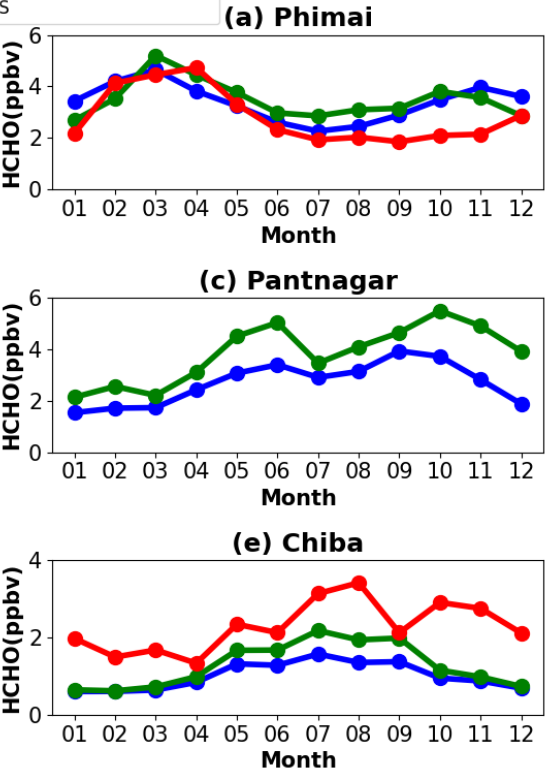


**Figure 14.** Seasonal variation in the surface HCHO and NO<sub>2</sub> mixing ratios at (a & b) Phimai, (c & d) Pantnagar, and (e & f) Chiba simulated at spatial resolutions of 2.8° × 2.8° (blue) and 1.4° × 1.4° (green). Coincident MAX-DOAS NO<sub>2</sub> and HCHO VMRs in the 0-1 km layer at Phimai and Chiba are plotted in red. Observation at Pantnagar are discarded. Only the datasets for 2017 are plotted.

1018  
1019  
1020  
1021  
1022  
1023  
1024  
1025  
1026  
1027  
1028  
1029  
1030  
1031  
1032  
1033  
1034  
1035  
1036  
1037  
1038

**Table 9:** The comparison between the observations and simulations at 2.8° and 1.4° spatial resolutions. The MBE is the mean bias error. The unit of MBE is ppbv.

Site	Trace gas	MBE at 2.8°	MBE at 1.4°	Differences between the simulations
Phimai	HCHO	0.54	0.65	3%
Phimai	NO <sub>2</sub>	0.33	0.43	9%
Chiba	HCHO	-1.27	-1.00	19%
Chiba	NO <sub>2</sub>	-0.52	-3.69	61%
Pantnagar				30%
Pantnagar				3%

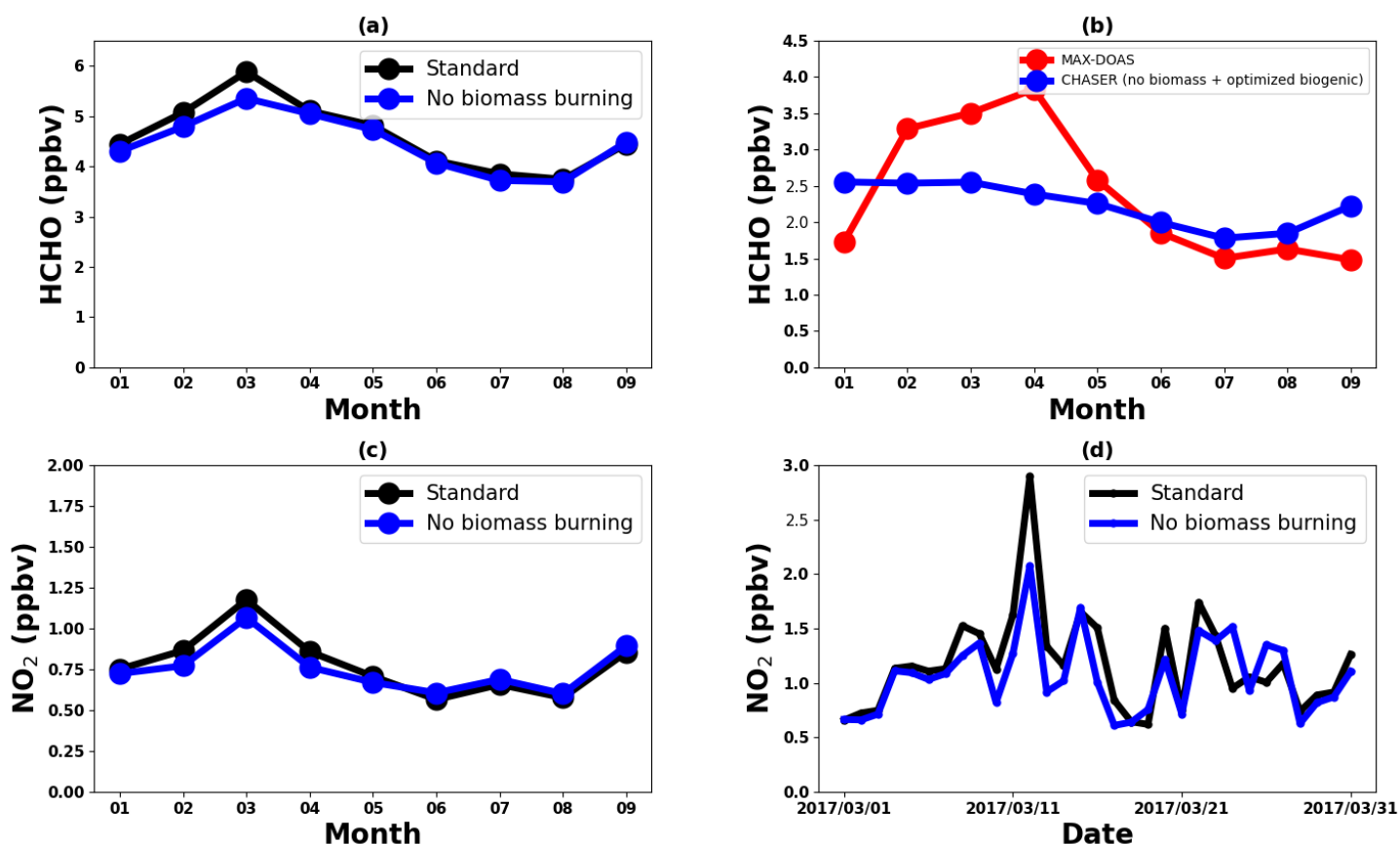
**3.4 Contribution estimates**

**3.4.1 Contribution from biomass burning to the HCHO and NO<sub>2</sub> abundances at Phimai**

Good agreement between the datasets in the 0 - 1 km layer at Phimai can quantify biomass burning contributions to the HCHO and NO<sub>2</sub> concentrations. Figure 15 presents results of simulations L1\_HCHO, L1\_opt, and L1\_NO<sub>2</sub>. The simulation settings are presented in Table 3. For better readability, the switched-off emissions criterion is described in the legends of Fig.15. The plots present mean mixing ratios in the 0 – 1 km layer. Biomass burning contributes ~10% to the HCHO concentrations at Phimai during the dry season. However, based on the observations, a greater effect of biomass burning is expected. During the wet season, the MAX-DOAS and CHASER HCHO surface mixing ratios are, respectively, ~2 and ~4 ppbv (Fig. 10), indicating overestimation of the biogenic emissions in CHASER. Figure 15(b) shows the HCHO concentration obtained from simulation L1\_opt and MAX-DOAS

1039 observations in 2017. In the L1\_opt simulation setting, the biomass burning emissions are switched off;  
 1040 the biogenic emissions are optimized to reproduce results analogous to those obtained from observations  
 1041 during the wet season. In the absence of biomass burning, the surface HCHO concentrations at Phimai  
 1042 would be ~2 ppbv, indicating a biomass burning contribution of ~20–50% during the dry season. The  
 1043 observed interseason difference in the HCHO concentration at Phimai is ~60%. Consequently, the revised  
 1044 biomass burning contribution estimate is more reasonable. Pyrogenic emissions contributions to the NO<sub>2</sub>  
 1045 concentrations at Phimai are ~10% during the dry season (Fig. 15(c)). Because the NO<sub>2</sub> concentrations  
 1046 are low at Phimai, the simulation results obtained for March, when the influence of biomass burning is  
 1047 highest, are used to derive a better contribution estimate. In the absence of biomass burning, the NO<sub>2</sub>  
 1048 concentration during March would be about 0.84 ppbv (Fig.15(d)), indicating a contribution as high as  
 1049 35% to the NO<sub>2</sub> concentrations at Phimai.

1050



1051

1052 **Figure 15.** (top panel) (a) Seasonal variations in the HCHO concentrations in the 0 - 1 km layer at Phimai, as  
1053 obtained from the standard and L1\_HCHO simulations. Pyrogenic emissions of VOCs are switched off in  
1054 L1\_HCHO. (b) The HCHO seasonal variation in Phimai in 2017, as obtained from the MAX-DOAS observations  
1055 (red) and L1\_opt simulations. The pyrogenic VOC emissions were switched off, and the biogenic emissions were  
1056 reduced by 50% in L1\_opt. The coincident dates between the observation and the simulations are shown only.  
1057 (bottom panel) (c) Seasonal variations in the NO<sub>2</sub> surface concentrations at Phimai in 2017, as obtained from the  
1058 standard and L1\_NO<sub>2</sub> simulations. (d) Standard and L1\_NO<sub>2</sub> simulation outputs of the daily mean NO<sub>2</sub> surface  
1059 concentrations during March 2017. The pyrogenic NO<sub>2</sub> emissions were switched off in the L1\_NO<sub>2</sub> simulation.  
1060 Only the daytime values from 09:00 – 15:00 LT are used to calculate the seasonal mean.

1061

1062

### 1063 **3.4.2 Contribution of soil NO<sub>x</sub> emissions at Phimai**

1064 Because soil NO<sub>x</sub> emissions are included in CHASER simulations, the NO<sub>2</sub> contributions from soil  
1065 emissions are quantified. Figure 16 presents the monthly mean surface NO<sub>2</sub> concentrations at Phimai in  
1066 2017, simulated including (standard) and switching off (L1\_NO<sub>2</sub>) the soil NO<sub>x</sub> emissions. The NO<sub>2</sub>  
1067 concentrations between 09 and 12 hr. were used to calculate the monthly mean concentrations. Soil  
1068 emissions contribute ~20% of the overall NO<sub>2</sub> concentrations at Phimai, with higher contributions during  
1069 the wet season. The highest soil contribution of about 25% occurs in July.

1070

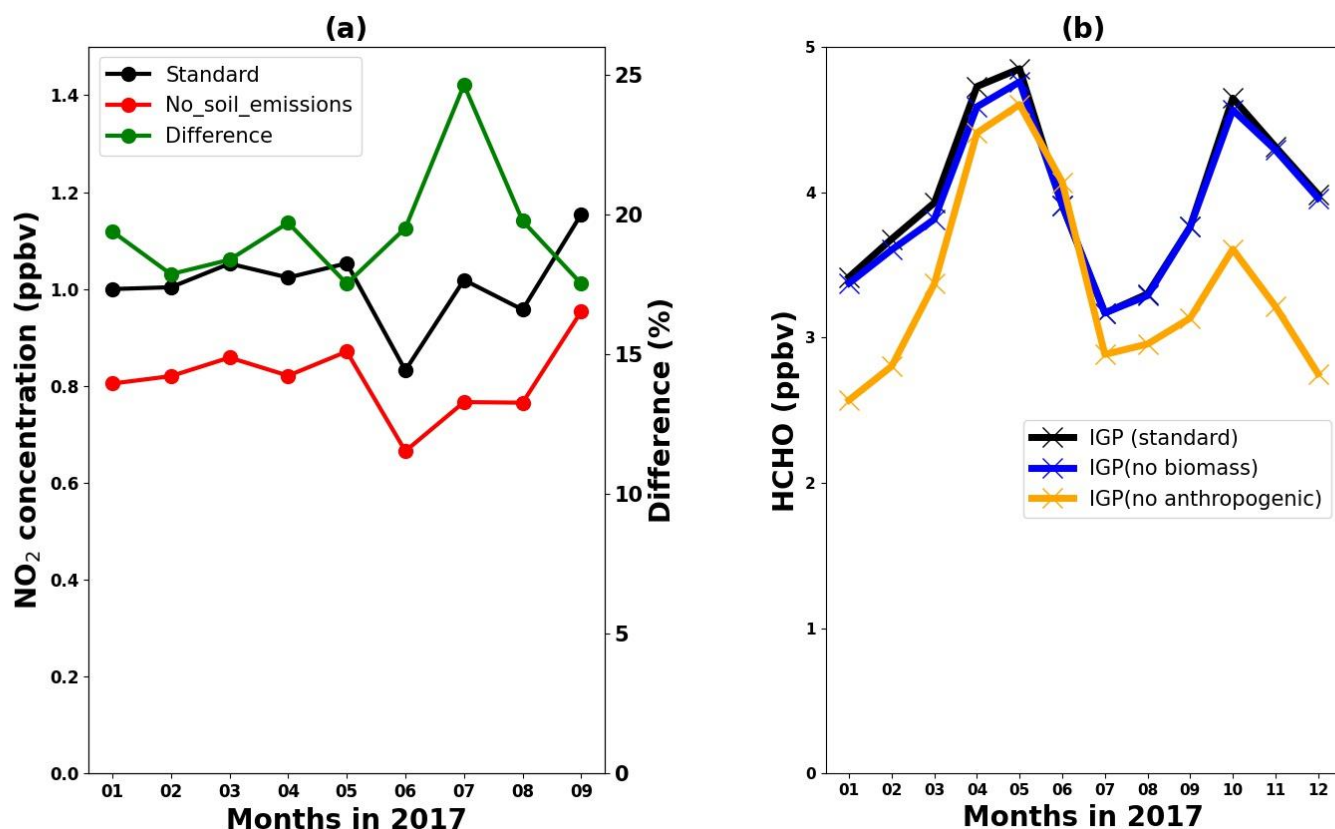
### 1071 **3.4.3 Contribution from pyrogenic and anthropogenic emissions to the HCHO abundances in the** 1072 **IGP region**

1073 Figure 16(b) presents the standard, L1\_HCHO (pyrogenic VOC emissions switched off), and L2  
1074 (anthropogenic VOC emissions switched off) HCHO simulations in the IGP region. According to  
1075 L1\_HCHO simulation results, effects of biomass burning emissions on the regional HCHO modulation  
1076 are small (~12%). The HCHO concentrations in India have biogenic, anthropogenic, and pyrogenic VOC  
1077 sources. However, biogenic VOCs are the primary driver of the over HCHO variation (Surl et al., 2018).  
1078 Consequently, two reasons might be responsible for the small effects of pyrogenic emissions on HCHO  
1079 concentrations: (1) Overestimation of the biogenic emission or underestimation of pyrogenic emissions

1080 in the model. (2) Stronger effects of anthropogenic VOC emissions than of pyrogenic VOCs. The L2  
 1081 simulations show that anthropogenic emissions contribute up to 30% of the HCHO concentration in the  
 1082 IGP region, with a maximum contributed during the post-monsoon season, which coincides with the  
 1083 lower isoprene concentration (i.e., biogenic emissions) and temperature (Fig. 14). Moreover, Kumar and  
 1084 Sinha (2021) reported high acetaldehyde concentrations from anthropogenic emissions in the IGP region  
 1085 throughout the year. Consequently, anthropogenic emissions are likely to be a significant driver of HCHO  
 1086 concentrations in the IGP region after biogenic emissions.

1087

1088



1089

1090 **Figure 16.** (a) Monthly mean  $\text{NO}_2$  concentrations at Phimai were estimated from the standard (black) and L1\_  $\text{NO}_2$   
 1091 (red) simulations. The soil  $\text{NO}_x$  emissions are switched off in the LI\_  $\text{NO}_2$  simulation. The green line represents the  
 1092 percentage difference between the two simulations. (b) Seasonal variations in the HCHO concentrations in the IGP

1093 region, obtained from the standard, L1\_HCHO (pyrogenic VOC emission switched off), and L2 simulations  
1094 (anthropogenic VOC emissions switched off). The simulations for 2017 are shown and analysed. Daytime values  
1095 from 09:00-12:00 and 09:00 – 15:00 LT were selected respectively, for Phimai and IGP.

1096

## 1097 **4 Conclusions**

1098 Using the JM2 algorithm, NO<sub>2</sub> and HCHO concentrations and profiles were retrieved from MAX-DOAS  
1099 observations at three A-SKY sites during January 2017 - December 2018. The retrieved products were  
1100 used to evaluate the global chemistry transport model CHASER simulations at the three sites. At all three  
1101 locations, the seasonal variation of both trace gases was consistent throughout the investigated period. At  
1102 Phimai and Pantnagar, biomass burning led to enhanced HCHO and NO<sub>2</sub> concentrations, respectively,  
1103 during the dry season and spring and post-monsoon season. At Chiba, the HCHO variation was consistent  
1104 with the temperature-led seasonal changes in biogenic emissions. The changes in the dry season HCHO  
1105 and NO<sub>2</sub> levels at Phimai during 2015 - 2018 were consistent with the number of fire events.

1106 The  $R_{FN}$  values were biased towards a particular regime when the standard transition range  $1 < R_{FN} < 2$   
1107 (Duncan et al., 2010) was used. The parameterization of Souri et al. (2020) provides a better estimate of  
1108 the transition region. The classification results of the revised transition region at Phimai and Pantnagar  
1109 contradicted the results based on the standard transition range. However, they were more reasonable. Such  
1110 a method based on observations, is therefore influenced by measurement constraints. More observational  
1111 evidence must be accumulated to standardize this method. Overall, the results further indicated that that  
1112 the standard transition region is not valid globally.

1113 Despite the use of an old NO<sub>x</sub> emission inventory the simulated NO<sub>2</sub> and HCHO spatial distributions  
1114 agreed reasonably well with those observed from satellite- observations. The modeled regional NO<sub>2</sub>  
1115 columns estimates were within the 2-sigma variability range of OMI NO<sub>2</sub> retrievals. Although the  
1116 negative bias in HCHO comparison was higher than that of NO<sub>2</sub>, the model demonstrated good  
1117 capabilities for simulating the HCHO seasonal variation in different regions.

1118 CHASER showed good capabilities at Phimai, characterized as a VOC-rich and low NO<sub>2</sub> (<1 ppbv)  
1119 region. In both seasons, the observed and modeled profiles (HCHO and NO<sub>2</sub>) agreed within the one sigma



1120 standard deviation of the measurements, despite general overestimation of the model. Furthermore, both  
1121 wet season HCHO profiles were almost identical in the 0.5 – 4 km layer in both datasets.  
1122 CHASER demonstrated limited performances at Chiba.NO<sub>2</sub> at higher resolution (i.e.,1.4°) mainly  
1123 improved the surface estimates, reducing the overall MBE in the 0 - 2 km layer by 35%. Finer resolution  
1124 would improve the HCHO estimates in Chiba by 10%; however, it has yet to be underestimated.  
1125 Sensitivity studies for the Phimai site estimated biomass burning contributions to the respective HCHO  
1126 and NO<sub>2</sub> concentrations up to ~50 and ~ 35%, respectively. On average, 20% of the NO<sub>2</sub> level originates  
1127 from soil NO<sub>x</sub> emissions, which increased to 25% in July. Anthropogenic emissions (contribution up to  
1128 30%) have a more strongly affect VOC variation in the IGP region than biomass burning, which is  
1129 consistent with reports presented in the literature.

1130

1131

1132 *Code availability.* The CHASER and JM2 source codes are not available publicly. Dr. Kengo Sudo  
1133 (kengo@nagoya-u.jp) is the contact person for readers and researchers interested in the CHASER model.  
1134 In addition, Dr. Hitoshi Irie (hitoshi.irie@chiba-u.jp) will answer queries related to the JM2 codes.

1135

1136 *Data availability:* The MAX-DOAS data used in the study are publicly accessible on the A-SKY network  
1137 website (<http://atmos3.cr.chiba-u.jp/a-sky/data.html>). Upon request, the corresponding author can  
1138 provide the CHASER simulations and MAX-DOAS averaging kernel data.

1139

1140 *Author contributions:* HMSH conceptualized the study, conducted the model simulations, analysed the  
1141 observational and simulation data, and drafted the manuscript. AMF helped with the data processing. HI  
1142 developed the JM2 code and maintained the A-SKY network. KS developed the CHASER model and  
1143 supervised the study. MN is the PI of the Pantnagar site. AD and MN shared their experience to explain  
1144 the results. HI, KS, AD, MN, and AMF commented and provided feedback on the final results and  
1145 manuscript.

1146

1147 *Conflict of Interest:* The authors declare that they have no conflict of Interest

1148

1149 *Acknowledgments:* This research is supported by the Global Environmental Research fund (S-12 and S-  
1150 20) of the Ministry of the Environment (MOE), Japan, and JSPS KAKENHI Grants: JP20H04320,  
1151 JP19HO5669, and JP19H04235. The CHASER model simulations are partly performed with the  
1152 supercomputer (NEC SX-Aurora TSUBASA) at the National Institute for environmental studies (NIES),  
1153 Tsukuba, Japan. The authors are grateful to the OMI and TROPOMI data providers. Support from ISRO-  
1154 ATCTM project for Pantnagar site is also acknowledged.

1155

1156

1157

## 1158 **References**

1159 Amnuaylojaroen, T., Inkom, J., Janta, R., & Surapipith, V. : Long range transport of southeast asian pm<sub>2.5</sub>  
1160 pollution to northern Thailand during high biomass burning episodes. *Sustainability*, 12(23), 10049. doi:  
1161 <https://doi.org/10.3390/su122310049>, 2020

1162

1163 Arlander, D., Brüning, D., Schmidt, U., and Ehhalt, D. : The tropospheric distribution of formaldehyde during  
1164 TROPOZ II, *J. Atmos. Chem.*, 22(3), 251-269, <https://doi.org/10.1007/BF00696637>, 1995

1165

1166 Bauwens, M, Verreyken, B, Stavrakou, T, Müller, JF, & De Smedt, I. : Spaceborne evidence for  
1167 significant anthropogenic VOC trends in Asian cities over 2005–2019. *Environ. Res. Lett.*, 17(1),  
1168 015008. doi:<https://iopscience.iop.org/article/10.1088/1748-9326/ac46eb/>, 2022

1169

1170

1171 Biswas, M. S., Ghude, S. D., Gurnale, D., Prabhakaran, T., and Mahajan, A. S. : Simultaneous Observations of  
1172 Nitrogen Dioxide, Formaldehyde and Ozone in the Indo-Gangetic Plain. *Aerosol Air Qual. Res.*, 19(8),  
1173 1749-1764, <https://doi.org/10.4209/aaqr.2018.12.0484>, 2019

1174

1175 Biswas, M. S., & Mahajan, A. S. : Year-long Concurrent MAX-DOAS Observations of Nitrogen Dioxide and  
1176 Formaldehyde at Pune: Understanding Diurnal and Seasonal Variation Drivers. *Aerosol Air Qual. Res.*,  
1177 21(6), 200524. doi:<https://doi.org/10.4209/aaqr.200524>, 2021

1178

1179

1180

1181 Boeke, N. L., Marshall, J. D., Alvarez, S., Chance, K. V., Fried, A., Kurosu, T. P., Rappengluck, B., Richter,  
1182 D., Walega, J., & Weibring, P. : Formaldehyde columns from the Ozone Monitoring Instrument: Urban  
1183 versus background levels and evaluation using aircraft data and a global model. J. Geophys. Res., 116(D5).  
1184 2011

1185

1186

1187

1188 Bond, D. W., Zhang, R., Tie, X., Brasseur, G., Huffman, G., Orville, R. E., and Boccippio, D. J. : NO<sub>x</sub> production  
1189 by lightning over the continental United States, J. Geophys. Res., 106(D21), 27701-27710,  
1190 <https://doi.org/10.1029/2000JD000191>, 2001

1191

1192 Bogumil, K., J. Orphal, T. Homann, S. Voigt, P. Spietz, O. Fleischmann, A. Vogel, M. Hartmann, H. Kromminga,  
1193 and H. Bovensmann : Measurements of molecular absorption spectra with the SCIAMACHY pre-flight  
1194 model: instrument characterization and reference data for atmospheric remote-sensing in the 230–2380 nm  
1195 region, J. Photochem. Photobiol. A, 157(2), 167-184, doi:10.1016/S1010-6030(03)00062-5, 2003

1196

1197

1198

1199

1200

1201 Burkert, J., Andrés-Hernández, M. D., Stöbener, D., Burrows, J. P., Weissenmayer, M., & Kraus, A. (2001) :  
1202 Peroxy radical and related trace gas measurements in the boundary layer above the Atlantic Ocean, J.  
1203 Geophys. Res., 106(D6), 5457-5477, <https://doi.org/10.1029/2000JD900613>, 2001

1204

1205

1206

1207 Cárdenas, L., Rondón, A., Johansson, C., & Sanhueza, E. : Effects of soil moisture, temperature, and inorganic  
1208 nitrogen on nitric oxide emissions from acidic tropical savannah soils. J. Geophys. Res., 98(D8), 14783-  
1209 14790, <https://doi.org/10.1029/93JD01020>, 1993

1210

1211 Chaliyakunnel, S., Millet, D. B., and Chen, X. : Constraining emissions of volatile organic compounds over the  
 1212 Indian subcontinent using space-based formaldehyde measurements. *J. Geophys. Res.*, 124(19), 10525-  
 1213 10545, <https://doi.org/10.1029/2019JD031262>, 2019  
 1214  
 1215  
 1216 Chance, K. V., and R. J. D. Spurr. : Ring effect studies: Rayleigh scattering, including molecular  
 1217 parameters for rotational Raman scattering: and the Fraunhofer spectrum, *Appl. Opt.* , 36(21),  
 1218 5224-5230 doi:10.1364/AO.36.005224,1997  
 1219  
 1220 Chutia, L., Ojha, N., Girach, I. A., Sahu, L. K., Alvarado, L. M. A., Burrows, J. P., Pathak., P., & Bhuyan, P. K. :  
 1221 Distribution of volatile organic compounds over Indian subcontinent during winter: WRF-chem simulation  
 1222 versus observations. *Environ. Pollut.*, 252, 256-269. doi:<https://doi.org/10.1016/j.envpol.2019.05.097>,  
 1223 2019  
 1224  
 1225  
 1226  
 1227 Clémer, K., Van Roozendaal, M., Fayt, C., Hendrick, F., Hermans, C., Pinardi, G., Spurr, R., Wang, P., and De  
 1228 Mazière, M. : Multiple wavelength retrieval of tropospheric aerosol optical properties from MAXDOAS  
 1229 measurements in Beijing, *Atmos. Meas. Tech.*, 3(4), 863-878, <https://doi.org/10.5194/amt-3-863-2010>,  
 1230 2010  
 1231  
 1232  
 1233 Colella, P., & Woodward, P. R. : The piecewise parabolic method (PPM) for gas-dynamical simulations. *J. Comput.*  
 1234 *Phys.*, 54(1), 174-201, [https://doi.org/10.1016/0021-9991\(84\)90143-8](https://doi.org/10.1016/0021-9991(84)90143-8), 1984  
 1235  
 1236  
 1237  
 1238  
 1239 Crutzen, P. J. : The influence of nitrogen oxides on the atmospheric ozone content. *Q. J. Roy. Meteor. Soc.*, 96(408),  
 1240 320-325, <https://doi.org/10.1002/qj.49709640815>, 1970  
 1241  
 1242

Davidson, E. A., Vitousek, P. M., Matson, P. A., Riley, R., García-Méndez, G., & Maass, J. M. : Soil emissions of  
 nitric oxide in a seasonally dry tropical forest of Mexico. *J. Geophys. Res.*, 96(D8), 15439-15445,  
<https://doi.org/10.1029/91JD01476>, 1991

De Smedt, I. , Pinardi, G., Vigouroux, C., Compernelle, S., Bais, A., Benavent, N., Eichmann, K-U., Hedelt, P.,  
 Hendricks, F., Irie, H., Kumar, V., Lambert, J-C., Langerock, B., Lerot, C., Liu, C., Loyola, D., Pitters, A.,  
 Richter, A., Cardens, C.R., Romahn, F., Ryan, R.G., Sinha, V., Theys, N., Vlietinck, J., Waggoner, T., Wang,  
 T., YU, H., and Van Roozendaal, M.,: Comparative assessment of TROPOMI and OMI formaldehyde  
 observations and validation against MAX-DOAS network column measurements. *Atmos. Chem. Phys.*,  
 21(16), 12561-12593. doi:<https://doi.org/10.5194/acp-21-12561-2021>, 2021

Duncan, B. N., Yoshida, Y., Damon, M. R., Douglass, A. R., and Witte, J. C. : Temperature dependence of factors  
 controlling isoprene emissions. *Geophys. Res. Lett.*, 36(5), <https://doi.org/10.1029/2008GL037090>, 2009

Emori, S., Nozawa, T., Numaguti, A., & Uno, I. : Importance of cumulus parameterization for precipitation  
 simulation over East Asia in June. *J. Meteorol. Soc. Jpn.*, 79(4), 939-947.  
<https://doi.org/10.2151/jmsj.79.939>, 2001

Fleischmann, O. C., M. Hartmann, J. P. Burrows, and J. Orphal : New ultraviolet absorption cross-sections of BrO  
 at atmospheric temperatures measured by time-windowing Fourier transform spectroscopy, *J. Photocho.*  
*Photobio. A*, 168(1), 117-132, doi:10.1016/j.jphotochem.2004.03.026, 2004

1275 Franco, B., Hendrick, F., Van Roozendaal, M., Müller, J.-F., Stavrakou, T., Marais, E. A., Bovy, B., Bader, W.,  
 1276 Fayt, C., Hermans, C., Lejuene, B., Pinardi, G., Sevais, C., and Mahieu, E. : Retrievals of formaldehyde  
 1277 from ground-based FTIR and MAX-DOAS observations at the Jungfraujoch station and comparisons with  
 1278 GEOS-Chem and IMAGES model simulations. *Atmos. Meas. Tech.*, 8(4), 1733-1756,  
 1279 <https://doi.org/10.5194/amt-8-1733-2015>, 2015  
 1280  
 1281 Fu, T. M., Jacob, D. J., Wittrock, F., Burrows, J. P., Vrekoussis, M., and Henze, D. K. : Global budgets of  
 1282 atmospheric glyoxal and methylglyoxal, and implications for formation of secondary organic aerosols, *J.*  
 1283 *Geophys. Res.*, 113(D15), <https://doi.org/10.1029/2007JD009505>, 2008  
 1284  
 1285  
 1286 Frieß, U., Monks, P. S., Remedios, J. J., Rozanov, A., Sinreich, R., Wagner, T., & Platt, U. : MAX-DOAS O4  
 1287 measurements: A new technique to derive information on atmospheric aerosols: 2. Modeling studies. *J.*  
 1288 *Geophys. Res.*, 111(D14), <https://doi.org/10.1029/2005JD006618>, 2006  
 1289  
 1290 Frieß, U., Klein Baltink, H., Beirle, S., Clémer, K., Hendrick, F., Henzing, B., Irie, H., de Leeuw, G., Li, A.,  
 1291 Moerman, M. M., van Roozendaal, M., Shaiganfar, R., Wagner, T., Wang, Y., Xie, P., Yilmaz, S., and  
 1292 Zieger, P. : Intercomparison of aerosol extinction profiles retrieved from MAX-DOAS measurements.  
 1293 *Atmos. Meas. Tech.*, 9(7), 3205-3222, <https://doi.org/10.5194/amt-9-3205-2016>, 2016  
 1294  
 1295 Fukushima, A., Kanamori, H., & Matsumoto, J. : Regionality of long-term trends and interannual variation of  
 1296 seasonal precipitation over India. *Prog Earth Planet Sci*, 6(1), 1-20. doi:[https://doi.org/10.1186/s40645-](https://doi.org/10.1186/s40645-019-0255-4)  
 1297 019-0255-4, 2019  
 1298  
 1299  
 1300 Hak, C., Pundt, I., Trick, S., Kern, C., Platt, U., Dommen, J., Ordóñez, C., Prévôt, A. S. H., Junkermann, W.,  
 1301 Astorga-Lloréns, C., Larsen, B. R., Mellqvist, J., Strandberg, A., Yu, Y., Galle, B., Kleffmann, J., Lörzer,  
 1302 J. C., Braathen, G. O., and Volkamer, R. : Intercomparison of four different in-situ techniques for ambient  
 1303 formaldehyde measurements in urban air, *Atmos. Chem. Phys.*, 5(11), 2881-2900.  
 1304 <https://doi.org/10.5194/acp-5-2881-2005>, 2005  
 1305  
 1306

1307

1308 Hall, S. J., Matson, P. A., and Roth, P. M. : NO<sub>x</sub> emissions from soil: implications for air quality modeling in  
1309 agricultural regions. *Annu. Rev. Energy Environ.*, 21(1), 311-346.  
1310 <https://doi.org/10.1146/annurev.energy.21.1.311>, 1996

1311

1312

1313 Halla, J. D., Wagner, T., Beirle, S., Brook, J. R., Hayden, K. L., O'Brien, J. M., Ng, A., Majonis, D., Wenig, M.  
1314 O., and McLaren, R : Determination of tropospheric vertical columns of NO<sub>2</sub> and aerosol optical  
1315 properties in a rural setting using MAX-DOAS. *Atmos. Chem. Phys.*, 11(23), 12475-12498,  
1316 <https://doi.org/10.5194/acp-11-12475-2011>, 2011

1317

1318

1319 Hendrick, F., Müller, J.-F., Clémer, K., Wang, P., De Mazière, M., Fayt, C., Gielen, C., Hermans, C., Ma, J. Z.,  
1320 Pinardi, G., Stavrou, T., Vlemmix, T., and Van Roozendaal, M.: Four years of ground-based MAX-  
1321 DOAS observations of HONO and NO<sub>2</sub> in the Beijing area, *Atmos. Chem. Phys.*, 14(2), 765-781,  
1322 <https://doi.org/10.5194/acp-14-765-2014>, 2014

1323

1324

1325 Hermans, C., A. Vandaele, S. Fally, M. Carleer, R. Colin, B. Coquart, A. Jenouvrier, and M.-F. Merienne.  
1326 : Absorption cross-section of the collision-induced bands of oxygen from the UV to the NIR, in *Weakly*  
1327 *interacting molecular pairs: unconventional absorbers of radiation in the atmosphere*, edited, pp. 193-  
1328 202, Springer, 2003.

1329

1330

1331

1332 Hönninger, G., Friedeburg, C. v., and Platt, U. : Multi axis differential optical absorption spectroscopy (MAX-  
1333 DOAS), *Atmos. Chem. Phys.*, 4(1), 231-254, <https://doi.org/10.5194/acp-4-231-2004>, 2004

1334

1335 Hoque, H.M. S., Irie, H., and Damiani, A. (2018). First MAX-DOAS Observations of Formaldehyde and Glyoxal  
1336 in Phimai, Thailand. *J. Geophys. Res.*, 123(17), 9957-9975, <https://doi.org/10.1029/2018JD028480>, 2018a

1337

1338 Hoque, H. M. S., Irie, H., Damiani, A., Rawat, P., and Naja, M. : First simultaneous observations of formaldehyde  
1339 and glyoxal by MAX-DOAS in the Indo-Gangetic Plain region. *Sola.* , [https://doi.org/10.2151/sola.2018-](https://doi.org/10.2151/sola.2018-028)  
1340 028, 2018b

1341

1342

1343 Houweling, S., Dentener, F., and Lelieveld, J. : The impact of nonmethane hydrocarbon compounds on tropospheric  
1344 photochemistry. *J. Geophys. Res.*, 103(D9), 10673-10696, <https://doi.org/10.1029/97JD03582>, 1998

1345

1346

1347

1348 Huber, D. E., Steiner, A. L., & Kort, E. A. : Daily Cropland Soil NO<sub>x</sub> Emissions Identified by TROPOMI and  
1349 SMAP. *Geophys. Res. Lett.*, 47(22), e2020GL089949, <https://doi.org/10.1029/2020GL089949>, 2020

1350

1351

1352

1353 Irie, H., Kanaya, Y., Akimoto, H., Iwabuchi, H., Shimizu, A., & Aoki, K. : First retrieval of tropospheric aerosol  
1354 profiles using MAX-DOAS and comparison with lidar and sky radiometer measurements. *Atmos. Chem.*  
1355 *Phys.*, 8(2), 341-350, <https://doi.org/10.5194/acp-8-341-2008>, 2008a

1356 Irie, H., Kanaya, Y., Akimoto, H., Tanimoto, H., Wang, Z., Gleason, J. F., & Bucsela, E. J. : Validation of OMI  
1357 tropospheric NO<sub>2</sub> column data using MAX-DOAS measurements deep inside the North China Plain in  
1358 June 2006: Mount Tai Experiment 2006. *Atmos. Chem. Phys.*, 8(22), 6577-  
1359 6586, <https://doi.org/10.5194/acp-8-6577-2008>, 2008b.

1360

1361 Irie, H., Kanaya, Y., Akimoto, H., Iwabuchi, H., Shimizu, A., & Aoki, K. : Dual-wavelength aerosol vertical profile  
1362 measurements by MAX-DOAS at Tsukuba, Japan. *Atmos. Chem. Phys.*, 9(8), 2741-2749,  
1363 <https://doi.org/10.5194/acp-9-2741-2009>, 2009

1364

1365 Irie, H., Takashima, H., Kanaya, Y., Boersma, K., Gast, L., Wittrock, F., Brunner, D., Zhou, Y., Roozendael, M.  
1366 V. : Eight-component retrievals from ground-based MAX-DOAS observations. *Atmos. Meas. Tech.*, 4(6),  
1367 1027-1044, <https://doi.org/10.5194/amt-4-1027-2011>, 2011



1368

1369 Irie, H., Nakayama, T., Shimizu, A., Yamazaki, A., Nagai, T., Uchiyama, A., Zaizen, Y., Kagamitani, S.,  
1370 and Matsumi, Y. : Evaluation of MAX-DOAS aerosol retrievals by coincident observations using CRDS,  
1371 lidar, and sky radiometer in Tsukuba, Japan. *Atmos. Meas. Tech.*, 8(7), 2775-2788,  
1372 <https://doi.org/10.5194/amt-8-2775-2015>, 2015

1373

1374 Irie, H., Muto, T., Itahashi, S., Kurokawa, J., & Uno, I. : Turnaround of tropospheric nitrogen dioxide pollution  
1375 trends in China, Japan, and South Korea. *Sola*, 12, 170-174. doi: <https://doi.org/10.2151/sola.2016-035>,  
1376 2016

1377

1378

1379 Irie, H., Yonekawa, D., Damiani, A., Hoque, H.M.S, Sudo, K., & Itahashi, S.; Continuous multi-component MAX-  
1380 DOAS observations for the planetary boundary layer ozone variation analysis at Chiba and Tsukuba, Japan,  
1381 from 2013 to 2019. *Prog Earth Planet Sci*, 8(1), 1-11. doi:[https://doi.org/10.1186/s40645-021-00424-](https://doi.org/10.1186/s40645-021-00424-9)  
1382 9,2021

1383

1384

1385 Ito, A., and Inatomi, M. : Use of a process-based model for assessing the methane budgets of global terrestrial  
1386 ecosystems and evaluation of uncertainty. *Biogeosciences*, 9(2), 759-773. [https://doi.org/10.5194/bg-9-](https://doi.org/10.5194/bg-9-759-2012)  
1387 759-2012, 2012

1388

1389

1390 Iwabuchi, H. :Efficient Monte Carlo methods for radiative transfer modeling. *J. Atmos. Sci.*, 63(9), 2324-2339,  
1391 <https://doi.org/10.1175/JAS3755.1>, 2006

1392

1393

1394 Jang, M., and Kamens, R. M. : Characterization of secondary aerosol from the photooxidation of toluene in the  
1395 presence of NO<sub>x</sub> and 1-propene, *Environ. Sci. Technol.*, 35(18), 3626-3639.  
1396 <https://doi.org/10.1021/es010676+>, 2001

1397

1398

1399 Jin, X., Fiore, A. M., Murray, L. T., Valin, L. C., Lamsal, L. N., Duncan, B., Boersma, K.F., De Smedt, I., Abad,  
1400 G.G., Chance, K., and Tonnesen, G. : Evaluating a space-based indicator of surface ozone-NO<sub>x</sub>-VOC

sensitivity over midlatitude source regions and application to decadal trends. *J. Geophys. Res.*, 122(19), 10,439-410,461, <https://doi.org/10.1002/2017JD026720>, 2017

Jin, X., & Holloway, T. (2015). Spatial and temporal variability of ozone sensitivity over China observed from the Ozone Monitoring Instrument. *J. Geophys. Res.*, 120(14), 7229-7246. doi: <https://doi.org/10.1002/2015JD023250>

Jenkin, M.E., Young, J.C., & Rickard, A.R. : The MCM v3. 3.1 degradation scheme for isoprene. *Atmos. Chem. Phys.*, 15(20), 11433-11459. doi:<https://doi.org/10.5194/acp-15-11433-2015>, 2015

Joshi, H., Manish, N., Singh, K.P., Kumar, R., Bhardwaj, P., Babu, S.S., Satheesh, S.K., Moorthy, K.K., Chandola, H.C. : Investigations of aerosol black carbon from a semi-urban site in the Indo-Gangetic Plain region, *Atmos. Environ.*, 125, 346-359, <https://doi.org/10.1016/j.atmosenv.2015.04.007>, 2016.

K-1 model developers : K-1 Coupled GCM (MIROC) description, Tech .rep., Center for Climate System Research (University of Tokyo), National Institute for Environmental Studies, and Frontier Research Center for Global Change, available at : [http://ccsr.aori.u-tokyo.ac.jp/~hasumi/miroc\\_description.pdf](http://ccsr.aori.u-tokyo.ac.jp/~hasumi/miroc_description.pdf), 2004

Kanakidou, M., Seinfeld, J. H., Pandis, S. N., Barnes, I., Dentener, F. J., Facchini, M. C., Van Dingenen, R., Ervens, B., Nenes, A., Nielsen, C. J., Swietlicki, E., Putaud, J. P., Balkanski, Y., Fuzzi, S., Horth, J., Moortgat, G. K., Winterhalter, R., Myhre, C. E. L., Tsigaridis, K., Vignati, E., Stephanou, E. G., and Wilson, J. : Organic aerosol and global climate modelling: a review. *Atmos. Chem. Phys.*, 5(4), 1053-1123, <https://doi.org/10.5194/acp-5-1053-2005>

Kanaya, Y., Irie, H., Takashima, H., Iwabuchi, H., Akimoto, H., Sudo, K., Gu, M., Chong, J., Kim, Y. J., Lee, H., Li, A., Si, F., Xu, J., Xie, P.-H., Liu, W.-Q., Dzhola, A., Postolyakov, O., Ivanov, V., Grechko, E., Terpugova, S., and Panchenko, M.: Long-term MAX-DOAS network observations of NO<sub>2</sub> in Russia and Asia (MADRAS) during the period 2007–2012: instrumentation, elucidation of

climatology, and comparisons with OMI satellite observations and global model simulations. *Atmos. Chem. Phys.*, 14(15), 7909-7927, <https://doi.org/10.5194/acp-14-7909-2014>, 2014

Kannari, A., Tonooka, Y., Baba, T., & Murano, K. : Development of multiple-species 1km× 1km resolution hourly basis emissions inventory for Japan. *Atmos. Environ.*, 41(16), 3428-3439. doi:<https://doi.org/10.1016/j.atmosenv.2006.12.015>, 2007

Khodmanee, S., & Amnuaylojaroen, T., Impact of Biomass Burning on Ozone, Carbon Monoxide, and Nitrogen Dioxide in Northern Thailand. *Front. Environ. Sci.*, 9, 27. doi:<https://doi.org/10.3389/fenvs.2021.641877>, 2021

Kreher, K., Van Roozendaal, M., Hendrick, F., Apituley, A., Dimitropoulou, E., Frieß, U., Richter, A., Wagner, T., Lampel, J., Abuhassan, N., Ang, L., Anguas, M., Bais, A., Benavent, N., Bösch, T., Bogner, K., Borovski, A., Bruchkouski, I., Cede, A., Chan, K. L., Donner, S., Drosoglou, T., Fayt, C., Finkenzeller, H., Garcia-Nieto, D., Gielen, C., Gómez-Martín, L., Hao, N., Henzing, B., Herman, J. R., Hermans, C., Hoque, S., Irie, H., Jin, J., Johnston, P., Khayyam Butt, J., Khokhar, F., Koenig, T. K., Kuhn, J., Kumar, V., Liu, C., Ma, J., Merlaud, A., Mishra, A. K., Müller, M., Navarro-Comas, M., Ostendorf, M., Pazmino, A., Peters, E., Pinardi, G., Pinharanda, M., Pithers, A., Platt, U., Postolyakov, O., Prados-Roman, C., Puertedura, O., Querel, R., Saiz-Lopez, A., Schönhardt, A., Schreier, S. F., Seyler, A., Sinha, V., Spinei, E., Strong, K., Tack, F., Tian, X., Tiefengraber, M., Tirpitz, J.-L., van Gent, J., Volkamer, R., Vrekoussis, M., Wang, S., Wang, Z., Wenig, M., Wittrock, F., Xie, P. H., Xu, J., Yela, M., Zhang, C., and Zhao, X.: Intercomparison of NO<sub>2</sub>, O<sub>4</sub>, O<sub>3</sub> and HCHO slant column measurements by MAX-DOAS and zenith-sky UV–visible spectrometers during CINDI-2. *Atmos. Meas. Tech.*, 13(5), 2169-2208, <https://doi.org/10.5194/amt-13-2169-2020>, 2020

Kumar, V., Beirle, S., Dörner, S., Mishra, A. K., Donner, S., Wang, Y., Sinha, V., and Wagner, T. (2020). Long-term MAX-DOAS measurements of NO<sub>2</sub>, HCHO, and aerosols and evaluation of corresponding satellite data products over Mohali in the Indo-Gangetic Plain. *Atmos. Chem. Phys.*, 20(22), 14183-14235. doi:10.5194/acp-20-14183-2020

1468 Kumar, V., & Sinha, V. (2021), Season-wise analyses of VOCs, hydroxyl radicals and ozone formation chemistry  
 1469 over north-west India reveal isoprene and acetaldehyde as the most potent ozone precursors throughout the  
 1470 year. *Chemosphere*, 283, 131184. doi:<https://doi.org/10.1016/j.chemosphere.2021.131184>  
 1471  
 1472  
 1473 Kurucz, R. L., Furenlid, I., Brault, J., and Testerman, L. : Solar Flux Atlas from 296 to 1300 nm.  
 1474 *Natl. Sol. Obs., Sunspot, New Mexico*, 240, 1984  
 1475  
 1476 Lee, M., Heikes, B. G., Jacob, D. J., Sachse, G., and Anderson, B. : Hydrogen peroxide, organic hydroperoxide,  
 1477 and formaldehyde as primary pollutants from biomass burning, *J. Geophys. Res.*, 102(D1), 1301-1309,  
 1478 <https://doi.org/10.1029/96JD01709>, 1997  
 1479  
 1480  
 1481  
 1482  
 1483  
 1484  
 1485  
 1486  
 1487  
 1488 Lin, S.-J., & Rood, R. B. : Multidimensional flux-form semi-Lagrangian transport schemes. *Mon. Weather Rev.*,  
 1489 124(9), 2046-2070, [https://doi.org/10.1175/1520-0493\(1996\)124<2046:MFFSLT>2.0.CO;2](https://doi.org/10.1175/1520-0493(1996)124<2046:MFFSLT>2.0.CO;2), 1996  
 1490  
 1491 Ma, J., Beirle, S., Jin, J., Shaiganfar, R., Yan, P., and Wagner, T. : Tropospheric NO<sub>2</sub> vertical column densities  
 1492 over Beijing: results of the first three years of ground-based MAX-DOAS measurements (2008–2011) and  
 1493 satellite validation, *Atmos. Chem. Phys.*, 13(3), 1547-1567, <https://doi.org/10.5194/acp-13-1547-2013>,  
 1494 2013  
 1495  
 1496  
 1497 Mallik, C., & Lal, S. : Seasonal characteristics of SO<sub>2</sub>, NO<sub>2</sub>, and CO emissions in and around the Indo-Gangetic  
 1498 Plain, *Environ Monit Assess*, 186(2), 1295-1310, <https://doi.org/10.1007/s10661-013-3458-y>, 2015

1499

1500 Martin, R. V., Fiore, A. M., and Van Donkelaar, A. : Space-based diagnosis of surface ozone sensitivity to  
1501 anthropogenic emissions, *Geophys. Res. Lett.*, 31(6), <https://doi.org/10.1029/2004GL019416>, 2004

1502

1503

1504 Mahajan, A. S., De Smedt, I., Biswas, M. S., Ghude, S., Fadnavis, S., Roy, C., and van Roozendaal, M. : Inter-  
1505 annual variations in satellite observations of nitrogen dioxide and formaldehyde over India. *Atmos.*  
1506 *Environ.*, 116, 194-201, <https://doi.org/10.1016/j.atmosenv.2015.06.004>, 2015

1507

1508

1509

1510

1511

1512

1513

1514 Meller, R., and G. K. Moortgat. : Temperature dependence of the absorption cross sections of formaldehyde  
1515 between 223 and 323 K in the wavelength range 225–375 nm, *J. Geophys. Res.*, 105(D6), 7089-7101,  
1516 doi:10.1029/1999JD901074, 2000

1517

1518

1519

1520 Mellor, G. L., & Yamada, T. : A hierarchy of turbulence closure models for planetary boundary layers. *J. Atmos.*  
1521 *Sci.*, 31(7), 1791-1806, [https://doi.org/10.1175/1520-0469\(1974\)031<1791:AHOTCM>2.0.CO;2](https://doi.org/10.1175/1520-0469(1974)031<1791:AHOTCM>2.0.CO;2), 1974

1522

1523

1524 Mishra, A. K., and Sinha, V. : Emission drivers and variability of ambient isoprene, formaldehyde and  
1525 acetaldehyde in north-west India during monsoon season, *Environ. Pollut.*, 267, 115538,  
1526 <https://doi.org/10.1016/j.envpol.2020.115538>, 2020

1527

1528 Miyazaki, K., Bowman, K., Sekiya, T., Eskes, H., Boersma, F., Worden, H., Livesey, N., Payne, V.H., Sudo, K.,  
1529 Kanaya, Y., Takigawa, M., and Ogochi, K. (2020). Updated tropospheric chemistry reanalysis and

emission estimates, TCR-2, for 2005–2018. *Earth Syst. Sci. Data*, 12(3), 2223-2259. doi:10.5194/essd-12-2223-2020

Miyazaki, K., Eskes, H., Sudo, K., Boersma, K. F., Bowman, K., and Kanaya, Y. : Decadal changes in global surface NO<sub>x</sub> emissions from multi-constituent satellite data assimilation. *Atmos. Chem. Phys.*, 17(2), 807-837, <https://doi.org/10.5194/acp-17-807-2017>, 2017

Morino, Y., Ohara, T., Yokouchi, Y., & Ooki, A. : Comprehensive source apportionment of volatile organic compounds using observational data, two receptor models, and an emission inventory in Tokyo metropolitan area. *J. Geophys. Res.*, 116(D2),doi:<https://doi.org/10.1029/2010JD014762>, 2011

Nair, V. S., Moorthy, K. K., Alappattu, D. P., Kunhikrishnan, P.K., George, S., Nair, P. R., Babu, S.S., Abish, A., Satheesh, S.K., Tripathi, S. N., Niranjana, K., Madhavan, B.L., Srikant, V., Dutt, C.B.S., Badarinath, K>V>S., & Reddy, R.R.: Wintertime aerosol characteristics over the Indo-Gangetic Plain (IGP): Impacts of local boundary layer processes and long-range transport. *J. Geophys. Res.*, 112(D13). doi:<https://doi.org/10.1029/2006JD008099>, 2007

Ohara, T., Akimoto, H., Kurokawa, J., Horii, N., Yamaji, K., Yan, X., & Hayasaka, T. : An Asian emission inventory of anthropogenic emission sources for the period 1980–2020. *Atmos. Chem. Phys.*, 7(16), 4419-4444. doi:<https://doi.org/10.5194/acp-7-4419-2007>, 2007

Platt, U. : Differential optical absorption spectroscopy (DOAS), in *Chemical Analysis Series*, edited, pp. 27-84, Wiley & Sons. Inc., 1994

Platt, U., and Stutz, J. : *Differential Optical Absorption Spectroscopy*, Springer, 2008

Price, C., & Rind, D. : A simple lightning parameterization for calculating global lightning distributions. *J. Geophys. Res.*, 97(D9), 9919-9933, <https://doi.org/10.1029/92JD00719>, 1992

Rodgers, C. D. : *Inverse methods for atmospheric sounding: theory and practice*, World scientific Singapore, 2008

1566 Roscoe, H. K., Van Roozendaal, M., Fayt, C., du Piesanie, A., Abuhassan, N., Adams, C., Akrami, M., Cede, A.,  
 1567 Chong, J., Clémer, K., Friess, U., Gil Ojeda, M., Goutail, F., Graves, R., Griesfeller, A., Grossmann, K.,  
 1568 Hemerijckx, G., Hendrick, F., Herman, J., Hermans, C., Irie, H., Johnston, P. V., Kanaya, Y., Kreher, K.,  
 1569 Leigh, R., Merlaud, A., Mount, G. H., Navarro, M., Oetjen, H., Pazmino, A., Perez-Camacho, M., Peters,  
 1570 E., Pinardi, G., Puentedura, O., Richter, A., Schönhardt, A., Shaiganfar, R., Spinei, E., Strong, K.,  
 1571 Takashima, H., Vlemmix, T., Vrekoussis, M., Wagner, T., Wittrock, F., Yela, M., Yilmaz, S., Boersma,  
 1572 F., Hains, J., Kroon, M., Piter, A., and Kim, Y. J. : Intercomparison of slant column measurements of NO<sub>2</sub>  
 1573 and O<sub>4</sub> by MAX-DOAS and zenith-sky UV and visible spectrometers. *Atmos. Meas. Tech.*, 3(6), 1629-  
 1574 1646, <https://doi.org/10.5194/amt-3-1629-2010>, 2010  
 1575  
 1576  
 1577 Ryan, R. G., Rhodes, S., Tully, M., & Schofield, R. : Surface ozone exceedances in Melbourne, Australia are  
 1578 shown to be under NO<sub>x</sub> control, as demonstrated using formaldehyde: NO<sub>2</sub> and glyoxal: formaldehyde  
 1579 ratios, *Sci. Total Environ.*, 749, 141460, <https://doi.org/10.1016/j.scitotenv.2020.141460>, 2020  
 1580  
 1581 Sadavarte, P., & Venkataraman, C. : Trends in multi-pollutant emissions from a technology-linked inventory for  
 1582 India: I. Industry and transport sectors. *Atmos. Environ.*, 99, 353-364.  
 1583 doi:<https://doi.org/10.1016/j.atmosenv.2014.09.081>, 2014  
 1584  
 1585 Sarmah, S., Singha, M., Wang, J., Dong, J., Burman, P. K. D., Goswami, S., Ge. Y., Ilyas, S., & Niu, S. :  
 1586 Mismatches between vegetation greening and primary productivity trends in South Asia—A satellite  
 1587 evidence. *Int. J. Appl. Earth Obs.*, 104, 102561. doi:<https://doi.org/10.1016/j.jag.2021.102561>, 2021  
 1588  
 1589  
 1590 Schindlbacher, A., Zechmeister-Boltenstern, S., & Butterbach-Bahl, K. : Effects of soil moisture and temperature  
 1591 on NO, NO<sub>2</sub>, and N<sub>2</sub>O emissions from European forest soils. *J. Geophys. Res.*, 109(D17),  
 1592 <https://doi.org/10.1029/2004JD004590>, 2004  
 1593  
 1594 Schroeder, J. R., Crawford, J. H., Fried, A., Walega, J., Weinheimer, A., Wisthaler, A., Muller, M., Mikovinu, T.,  
 1595 Chen, G., Shook, M. : New insights into the column CH<sub>2</sub>O/NO<sub>2</sub> ratio as an indicator of near-surface ozone  
 1596 sensitivity. *J. Geophys. Res.*, 122(16), 8885-8907. doi: <https://doi.org/10.1002/2017JD026781>, 2017  
 1597  
 1598 Sharma, S., Goel, A., Gupta, D., Kumar, A., Mishra, A., Kundu, S., Chatani, S., and Klimont, Z. : Emission  
 1599 inventory of non-methane volatile organic compounds from anthropogenic sources in India. *Atmos.*  
 1600 *Environ.*, 102, 209-219. doi:<https://doi.org/10.1016/j.atmosenv.2014.11.070>, 2015

1601  
 1602  
 1603  
 1604 Seco, R., Penuelas, J., and Filella, I. : Short-chain oxygenated VOCs: Emission and uptake by plants and  
 1605 atmospheric sources, sinks, and concentrations, *Atmos. Environ.*, 41(12), 2477-2499,  
 1606 <https://doi.org/10.1016/j.atmosenv.2006.11.029>, 2007  
 1607  
 1608  
 1609  
 1610 Sekiya, T., & Sudo, K. : Roles of transport and chemistry processes in global ozone change on interannual and  
 1611 multidecadal time scales. *J. Geophys. Res.*, 119(8), 4903-4921.  
 1612 doi:<https://doi.org/10.1002/2013JD020838>, 2014  
 1613  
 1614 Sekiya, T., Miyazaki, K., Ogochi, K., Sudo, K., & Takigawa, M. : Global high-resolution simulations of  
 1615 tropospheric nitrogen dioxide using CHASER V4.0. *Geosci. Model Dev.*, 11(3), 959-988.  
 1616 <http://doi.org/10.5194/gmd-11-959-2018>, 2018  
 1617  
 1618 Seinfeld, J. H., & Pandis, S. N. : Atmospheric chemistry and physics: from air pollution to climate change: John  
 1619 Wiley & Sons, New York, 1998  
 1620  
 1621 Sindelarova, K., Markova, J., Simpson, D., Huszar, P., Karlicky, J., Darras, S., & Granier, C. : High-resolution  
 1622 biogenic global emission inventory for the time period 2000–2019 for air quality modelling. *Earth Syst.*  
 1623 *Sci. Data*, 14(1), 251-270. doi:<https://doi.org/10.5194/essd-14-251-2022>, 2022  
 1624  
 1625 Singh, H., Salas, L., Chatfield, R., Czech, E., Fried, A., Walega, J., Evans, M.J., Field, B.D., Jacob, D.J., Blake,  
 1626 D., Heikes, B., Talbott, R., Sachse, G., Crawford, J.H., Avery, M.A., Sandholm, S., and Fuelberg, H. :  
 1627 Analysis of the atmospheric distribution, sources, and sinks of oxygenated volatile organic chemicals based  
 1628 on measurements over the Pacific during TRACE-P, *J. Geophys. Res.*, 109(D15),  
 1629 <https://doi.org/10.1029/2003JD003883>, 2004  
 1630



1631 Sinreich, R., Frieß, U., Wagner, T., and Platt, U. : Multi axis differential optical absorption spectroscopy (MAX-  
 1632 DOAS) of gas and aerosol distributions, Faraday discuss., 130, 153-164,  
 1633 <https://doi.org/10.1039/B419274P>, 2005  
 1634  
 1635  
 1636 Solomon, S., Portmann, R., Sanders, R., Daniel, J., Madsen, W., Bartram, B., and Dutton, E. : On the role of  
 1637 nitrogen dioxide in the absorption of solar radiation, J. Geophys. Res., 104(D10), 12047-12058,  
 1638 <https://doi.org/10.1029/1999JD900035>, 1999  
 1639  
 1640  
 1641 Souri, A. H., Nowlan, C. R., Wolfe, G. M., Lamsal, L. N., Miller, C. E. C., Abad, G. G., Janz, S., Fried, A., Blake,  
 1642 D. R., Weinheimer, A. J. , Diskin, G.S., Liu, X., and Chance, K. : Revisiting the effectiveness of  
 1643 HCHO/NO<sub>2</sub> ratios for inferring ozone sensitivity to its precursors using high resolution airborne remote  
 1644 sensing observations in a high ozone episode during the KORUS-AQ campaign. Atmos. Environ., 224,  
 1645 117341, <https://doi.org/10.1016/j.atmosenv.2020.117341>, 2020  
 1646  
 1647  
 1648 Sudo, K., & Akimoto, H. (2007). Global source attribution of tropospheric ozone: Long-range transport from  
 1649 various source regions. J. Geophys. Res., 112(D12), <https://doi.org/10.1029/2006JD007992>, 2007  
 1650  
 1651 Sudo, K., Takahashi, M., Kurokawa, J., & Akimoto, H. : CHASER: A global chemical model of the troposphere  
 1652 1. Model description. J. Geophys. Res., 107, 4339, <https://doi.org/10.1029/2001JD001113>, 2002  
 1653  
 1654 Surl, L., Palmer, P. I., & González Abad, G. : Which processes drive observed variations of HCHO columns over  
 1655 India? Atmos. Chem. Phys., 18(7), 4549-4566 ,<https://doi.org/10.5194/acp-18-4549-2018>, 2018  
 1656  
 1657  
 1658 Takemura, T., Nozawa, T., Emori, S., Nakajima, T. Y., & Nakajima, T. : Simulation of climate response to aerosol  
 1659 direct and indirect effects with aerosol transport-radiation model. J. Geophys. Res., 110(D2),  
 1660 <https://doi.org/10.1029/2004JD005029>, 2005  
 1661

1662 Takemura, T., Egashira, M., Matsuzawa, K., Ichijo, H., O'ishi, R., & Abe-Ouchi, A. : A simulation of the global  
 1663 distribution and radiative forcing of soil dust aerosols at the Last Glacial Maximum. *Atmos. Chem. Phys.*,  
 1664 9(9), 3061-3073, <https://doi.org/10.5194/acp-9-3061-2009>, 2009  
 1665  
 1666 Tonnesen, G. S., & Dennis, R. L. (2000). Analysis of radical propagation efficiency to assess ozone sensitivity to  
 1667 hydrocarbons and NO<sub>x</sub>: 1. Local indicators of instantaneous odd oxygen production sensitivity. *J. Geophys.*  
 1668 *Res.*, 105(D7), 9213-9225. doi:<https://doi.org/10.1029/1999JD900371>  
 1669  
 1670  
 1671 Vandaele, A., C. Hermans, P. Simon, M. Van Roozendael, J. Guilmot, M. Carleer, and R. Colin.: Fourier  
 1672 transform measurement of NO<sub>2</sub> absorption cross-section section in the visible range at room temperature,  
 1673 *J. Atmos. Chem.*, 25(3), 289-305, doi:10.1007/BF00053797, 2009  
 1674  
 1675  
 1676 Vandaele, A. C., C. Fayt, F. Hendrick, C. Hermans, F. Humbled, M. V. Roozendael, M. Gil, M. Navarro, O.  
 1677 Puertedura, M. Yela, G. Braathen, K. Stebel, K. Tornkvist, P. Jhonston, K. Kreher, F. Goutail, F. Mieville,  
 1678 J.P. Pommereau, S. Khaikine, A. Richter, H. Oetjen, F. Wittrock, S. Bugarski, U. Friess, K. Pfeilsticker,  
 1679 R. Sinreich, T. Wagner, G. Corlett, and R. Leigh ), An intercomparison campaign of ground-based UV-  
 1680 visible measurements of NO<sub>2</sub>, BrO, and OClO slant columns Methods of analysis and results for NO<sub>2</sub>, *J.*  
 1681 *Geophys Res*, 110(D8),2005  
 1682  
 1683  
 1684 Vigouroux, C., Hendrick, F., Stavrakou, T., Dils, B., De Smedt, I., Hermans, C., Merlaud, A., Scolas, F., Senten,  
 1685 C., Vanhaelewyn, G., Fally, S., Carleer, M., Metzger, J.-M., Müller, J.-F., Van Roozendael, M., and De  
 1686 Mazière, M.: Ground-based FTIR and MAX-DOAS observations of formaldehyde at Réunion Island and  
 1687 comparisons with satellite and model data, *Atmos. Chem. Phys.*, 9(24), 9523-9544,  
 1688 <https://doi.org/10.5194/acp-9-9523-2009>, 2009  
 1689  
 1690  
 1691  
 1692

1693 Wagner, T., Dix, B. v., Friedeburg, C. v., Frieß, U., Sanghavi, S., Sinreich, R., & Platt, U. : MAX-DOAS O4  
 1694 measurements: A new technique to derive information on atmospheric aerosols—Principles and  
 1695 information content. *J. Geophys. Res.*, 109(D22). doi: <https://doi.org/10.1029/2004JD004904>, 2004  
 1696  
 1697 Wagner, T., Burrows, J., Deutschmann, T., Dix, B., Friedeburg, C. v., Frieß, U., Iwabuchi, H. , Hendrick, F., Heue,  
 1698 K.-P., Irie, H., Iwabuchi, H., Kanaya, Y., Keller, J., McLinden, C. A., Oetjen, H., Palazzi, E., Petritoli, A.,  
 1699 Platt, U., Postlyakov, O., Pukite, J., Richter, A., van Roozendaal, M., Rozanov, A., Rozanov, V., Sinreich,  
 1700 R., Sanghavi, S., and Wittrock, F. : Comparison of box-air-mass-factors and radiances for Multiple-Axis  
 1701 Differential Optical Absorption Spectroscopy (MAX-DOAS) geometries calculated from different  
 1702 UV/visible radiative transfer models. *Atmos. Chem. Phys.*, 7(7), 1809-1833.  
 1703 doi:<https://doi.org/10.5194/acp-7-1809-2007>, 2007  
 1704  
 1705  
 1706 Wang, T., Hendrick, F., Wang, P., Tang, G., Clémer, K., Yu, H., Fayt, C., Hermans, C., Gielen, C., Müller, J.-F.,  
 1707 Pinardi, G., Theys, N., Brenot, H., and Van Roozendaal, M. : Evaluation of tropospheric SO<sub>2</sub> retrieved  
 1708 from MAX-DOAS measurements in Xianghe, China. *Atmos. Chem. Phys.*, 14(20), 11149-11164,  
 1709 <https://doi.org/10.5194/acp-14-11149-2014>, 2014  
 1710  
 1711  
 1712  
 1713  
 1714 Wesely, M. : Parameterization of surface resistances to gaseous dry deposition in regional-scale numerical models.  
 1715 *Atmos. Environ.*, 41, 52-63. <https://doi.org/10.1016/j.atmosenv.2007.10.058>, 1989  
 1716  
 1717 Williams, J. E., Boersma, K. F., Sager, P. L., & Verstraeten, W. W.. The high-resolution version of TM5-MP for  
 1718 optimized satellite retrievals: description and validation. *Geosci. Model Dev.*, 10(2), 721-750.  
 1719 doi:<https://doi.org/10.5194/gmd-10-721-2017>, 2017  
 1720  
 1721  
 1722 Wittrock, F., Oetjen, H., Richter, A., Fietkau, S., Medeke, T., Rozanov, A., and Burrows, J. : MAX-DOAS  
 1723 measurements of atmospheric trace gases in Ny-Ålesund-Radiative transfer studies and their application,  
 1724 *Atmos. Chem. Phys.*, 4(4), 955-966, <https://doi.org/10.5194/acp-4-955-2004>, 2004

1725  
1726  
1727  
1728  
1729  
1730  
1731  
1732  
1733  
1734

Woo, J-H., Kim, Y. , Kim, H-K., Choi, K-C., Eum, J-H., Lee, J-B., Lim, J-H., Kim,J., and Seong, M. : Development of the CREATE inventory in support of integrated climate and air quality modeling for Asia. Sustainability, 12(19), 7930. doi:<https://doi.org/10.3390/su12197930>, 2020